ECO-FRIENDLY SOLAR CELLS WITH CATION-ENGINEERED $AgBiS_2$ NANOCRYSTALS

Yongjie Wang

ICFO – The Institute of Photonic Sciences

Barcelona, 2022

ECO-FRIENDLY SOLAR CELLS WITH CATION-ENGINEERED $AgBiS_2$ NANOCRYSTALS

Yongjie Wang

Under the supervision of

Prof. Gerasimos Konstantatos

A thesis submitted in conformity with the requirements

for the degree of

Doctor of Philosophy in Photonics

By the

Universitat Politècnica de Catalunya

Barcelona, 2022

Abstract

Climate change and global energy demand urge the development of renewable energy sources for worldwide power supply. Photovoltaic devices that convert solar energy directly into electricity are the most promising, if not the only, technique to meet the requirements. Solution-processed solar cells are especially attractive due to their lightweight, low cost, and large-area mass manufacturing features.

Among solution-processed materials, nanocrystals are one of the most promising, thanks to their material-property tunabilities, such as size, morphology, composition, electronic and optical properties, just to name a few. In the last decade, nanocrystal solar cells are mainly based on lead chalcogenide nanocrystals, although they face problems related to the toxicity of the element lead. Silver-bismuth sulfide nanocrystals are excellent substitutes for lead chalcogenides, thanks to their adequate bandgaps and extraordinarily high absorption coefficients. However, the energy conversion efficiency has lagged behind their toxic counterparts, mainly due to limited charge-carrier diffusion length and uncontrolled cation-disorder.

In this thesis, we pinpoint the detrimental effects of cation inhomogeneity in ternary silver bismuth sulfide nanocrystals and further homogenize the cation-disorder by a facile post-annealing process, leading to absorption coefficients

higher than any other commonly used solar materials over a wide range of 400 - 1000 nm. The cation-disorder configuration transition was further confirmed by the combination of ab initio density functional theory calculation and experimental material characterizations.

Further optical modelling suggested a 30nm absorber layer possesses the potential for high J_{sc} up to 30 mA/cm^2 and efficiency up to 26%. In addition to optical absorption enhancements, we also found elongated diffusion length up annealing, pointing to an anticipated high performance with ultrathin absorber. Ultrathin solar cells were thus fabricated with specially designed architecture and we achieved a record efficiency up to 9.17%, independently certified as 8.85% by Newport. The ultrathin solar cells also showed excellent stability under ambient conditions.

In order to comply with mass manufacturing processes, we developed a solution-phase ligand-exchange procedure based on aqueous nanocrystal inks that enable single-step deposition of the active layer, reducing drastically the number of processing steps. Solar cell devices were built with the nanocrystal inks based on single-step deposition process and they showed a promising efficiency up to 7.3%, much higher than previous ink device record.

In sum, we have achieved record-high performance, exceptionally stable $AgBiS_2$ nanocrystal solar cells with both solid-state and solution-phase ligand-

exchange procedures. This work sets a landmark for the development of environmentally friendly, low-temperature, solution-processed inorganic solar cells and opens a new field of engineering the atomic configuration of semiconductors as a means to achieve extraordinary optoelectronic properties.

Resumen

El cambio climático y la demanda mundial de energía urgen el desarrollo de fuentes de energía renovables para el suministro de energía en todo el mundo. La generación de energía fotovoltaica, que consiste en la conversión de la energía solar directamente en electricidad, es el sistema más prometedor, sino el único, para satisfacer estas necesidades. La fabricación de células solares a partir de materiales en disolución es uno de los procesos emergentes especialmente atractivo por sus beneficiosas propiedades como la ligereza de los dispositivos, el bajo coste, la posibilidad de fabricación en masa, etc.

Entre los materiales procesados en solución, los nanocristales son extremadamente prometedores, gracias a su habilidad de modificar sus propiedades ópticas y electrónicas dependiendo de su tamaña, morfología y composición. En la última década, las células solares de nanocristales se han basado principalmente en nanocristales de calcogenuro de plomo, aunque estas presentan problemas relacionados con la toxicidad del elemento plomo. Los nanocristales de sulfuro de bismuto y plata pueden ser excelentes sustitutos de estos materiales, ya que tienen brechas de banda adecuadas y altos coeficientes de absorción. Sin embargo, la eficiencia de conversión de energía ha quedado por detrás de sus homólogos tóxicos, debido principalmente a que presentan una corta distancia de difusión y desorden catiónico descontrolado.

En esta tesis se han determinado los efectos perjudiciales de la heterogeneidad catiónica en los nanocristales ternarios de sulfuro de bismuto y plata y, además, se ha desarrollado un procedimiento de recocido sencillo para homogeneizar este desorden catiónico que permite obtener coeficientes de absorción ultra elevados, superiores a los de cualquier otro material de uso común en aplicaciones fotovoltaicas en un amplio rango de 400 a 1000 nm. La transición de la configuración catión-desorden se confirmó además mediante la combinación de cálculos de la teoría del funcional de la densidad ab initio y caracterizaciones experimentales del material.

Otros modelos ópticos sugirieron que una capa ultrafina absorbente de 30 nm posee el potencial para lograr un alto J_{sc} de hasta 30 mA/cm^2 y una eficiencia de hasta el 26%. Además de la mejora de la absorción óptica, se ha demostrado que después del tratamiento de recocido se elonga la distancia de difusión. Este resultado anticipa un alto rendimiento usando absorbentes ultrafinos. Las células solares ultrafinas se diseñaron y fabricaron con una arquitectura especial que alcanzó una eficiencia récord de hasta el 9,17%, certificada independientemente por NewPort como 8,85%. Asimismo, la célula solar ultrafina también mostró una excelente estabilidad en condiciones ambientales.

Con el fin de compatibilizarlo con los procesos de fabricación en masa, se ha desarrollado un procedimiento de intercambio de ligandos en fase de solución que nos permite obtener tintas acuosas de nanocristales. Los dispositivos de células solares se fabrican mediante un proceso de deposición de las tintas de nanocristales en un solo paso. Estos dispositivos mostraron una eficiencia de hasta el 7,3%, muy superior a los registros anteriores de dispositivos de tinta.

En resumen, se han fabricado celdas solares basadas en nanocristales de $AgBiS_2$ que alcanzon un rendimiento récord, a partir de dos métodos diferentes: un procedimiento en estado sólido y uno de intercambio de ligandos en disolución. Este trabajo marca un hito en el desarrollo de células solares inorgánicas respetuosas con el medio ambiente, de baja temperatura y procesadas en solución, y abre un nuevo campo de ingeniería de la configuración atómica de los semiconductores como medio para conseguir propiedades optoelectrónicas extraordinarias.

Acknowledgements

First, I would like to express my deepest gratitude to my supervisor, ***Prof.*** **Gerasimos Konstantatos**, for his extraordinary mentorship, endless support and patient guidance. I can always remember vividly the encouraged and motivated mood after every discussion. Your insight and passion also inspired me to be more efficient and diligent.

I am grateful to all our group members that I have met and worked with. I thank **Mariona** for always keeping the chemical lab cleaning as fresh, for her tremendous help and discussion about chemistries. I thank the ABS team members: **Zafer**, **Ignasi** and **Jae-Taek** for being fantastic partners to push the limit of ABS devices. I thank **Sean**, **David** and **Aron** for being wonderful collaborators and making great contributions into ABS projects.

I also would like to thank **Santanu** and **Sotirios** for being amazing officemates when I was starting a new journey at ICFO. I thank **Stephy**, **Adi** and **Yurong** for being the new-generation officemates with inspiring ideas.

I thank **Yu**, **Nengjie**, **Zhuoran** and **Lucheng** for sharing their rich knowledge and providing generous supports. I thank **Nima**, **Shanti**, **Alberto**, **Gaurav**, **Biswajit**, **Guy**, **Onur**, **Avijit**, **Iñigo**, **Debranjan**, **Hyun-Soo**, **Katerina**, **Huimin** and **Yuzhi** for all the help and fruitful discussions.

I would like to thank **my parents** and wife **Yunqi** for their love and encouragement, for their continuous support during the tough years.

Finally, I thank **ICFO**, **Barcelona Institute of Science and Technology (BIST)** and the **Marie Skłodowska-Curie grant** for financial support of the PREBIST PhD Fellowship Program.

List of Acronyms

NC	Nanocrystal
PCE, η	Power conversion efficiency
ETL	Electron transporting layer
HTL	Hole transporting layer
J_{sc}	Short circuit current density
V_{oc}	Open circuit voltage
FF	Fill factor
$AgBiS_2$	Silver bismuth sulfide
SLME	Spectroscopic limited maximum efficiency
TMM	Transfer matrix method
3-MPA	3-mercaptopropionic acid
VBM	Valence band maximum
CBM	Conduction band minimum
DOS	Density of states
DFT	Density functional theory
XRD	X-ray diffraction
HRTEM	High resolution transmission electron microscopy
XPS	X-ray photoelectron spectroscopy
UPS	Ultraviolet photoelectron spectroscopy
IQE	Internal quantum efficiency
PTB7	Poly[[4,8-bis[(2-ethylhexyl)oxy]benzo[1,2-b:4,5-b’] dithiophene-2,6-diyl][3-fluoro-2-[(2-ethylhexyl) carbonyl]

	thieno [3,4-b]thiophenediyl]]
PTAA	Poly(triaryl amine)
AFM	Atomic force microscopy
EQE	External quantum efficiency
MoO_x	Molybdenum oxide
MPP	Maximum power point
TPV	Transient photovoltage
TPC	Transient photocurrent
RoHS	Restrict of hazardous substance
SPLE	Solution-phase ligand-exchange
FA	Formamide
DMF	Dimethylformamide
DMSO	Dimethyl sulfoxide
MeOH	Methanol
OA	Oleic acid
FTIR	Fourier transform infrared spectroscopy
BA	Butyl amine
NMR	Nuclear magnetic resonance
VBO	Valence band offset
CBO	Conduction band offset
Photo-CELIV	Photo-charge extraction by linearly increased voltage

List of Figures and Tables

Table of Contents

Chapter 1 Introduction

Climate change and global energy demand

Climate change, especially global warming, brings profound impact to our daily lives. The global warming is mainly due to the emission of greenhouse gases, including carbon dioxide (CO_2) and methane. These greenhouse gases are transparent to sunlight, allowing the heat arriving on earth while they absorb the infrared light emitted by earth, blocking the heat dissipation and trapping the heat on the planet, causing global temperature arising.[1]

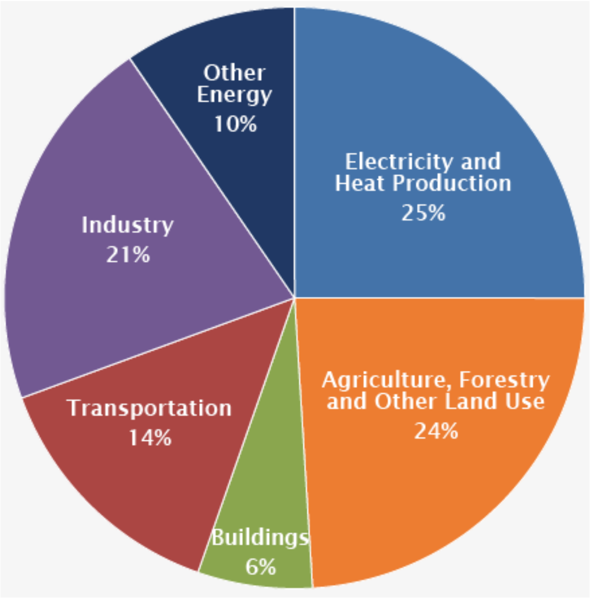

Figure 1.1 Global Greenhouse gas emissions by economic sector. *Copyright by United States Environmental Protection Agency.*

The energy section, the major source of greenhouse gas emissions[2], is the key to mitigate the global climate change (Fig. 1.1). Although governments have made policies and efforts to tackle the global warming, the greenhouse gas emissions have been keeping increasing since the 1992 United Nations Framework Convention on Climate Change. Global pledges and actions are growing, but they still fail to achieve what is needed to regulate the global temperatures rise to 1.5ºC and avoid the terrible consequences of climate change (Fig. 1.2).[3,4]

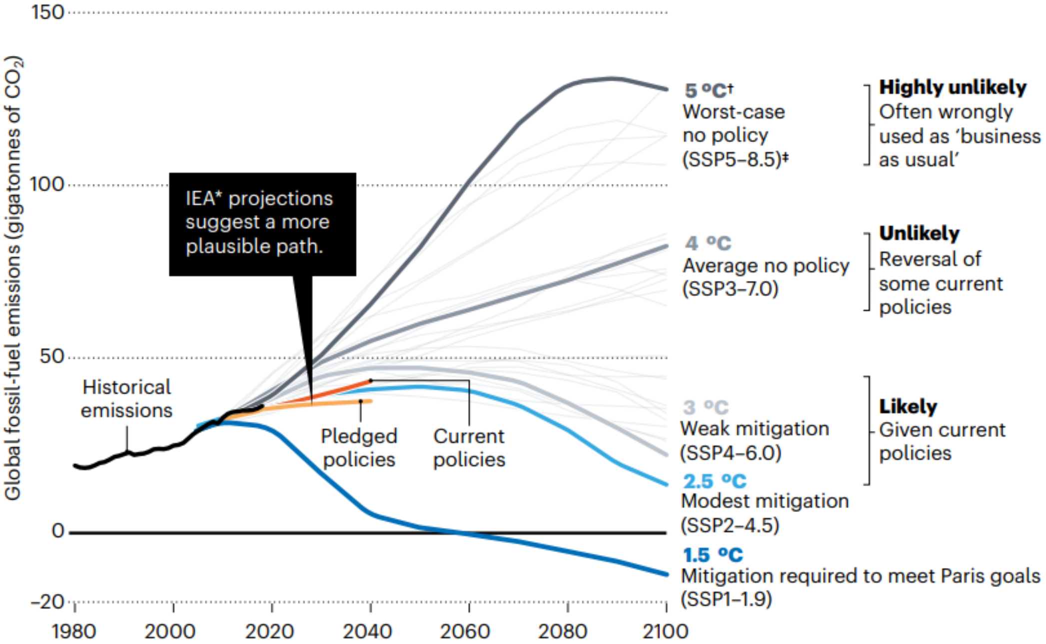

Figure 1.2 Possible futures. *Projected global temperature change with global CO$_2$ emissions. Figure adapted from ref [4], copyright by Nature Publishing Group.*

On the other hand, the global energy demand is increasing dramatically. The post-pandemic economic recovery demands higher energy consumption and leads to higher energy-related CO_2 emissions. The extreme heatwaves from climate change hit the northern hemisphere and intensified the demand for electricity in the summer of 2022. More fossil fuel are thus needed for electricity supply and in turn worsen the global warming, forming a vicious circle, if there is no other energy sources coming in.

The global energy crisis escalated by the Russia-Ukraine war in 2022 further urges many nations' decarbonization and energy independency on Russian fossil fuels. Renewable energy technologies like solar photovoltaics and wind farms are the keys to not only supplying sufficient energies, but also lowering greenhouse emissions in the electricity part, which is still the predominant source of CO_2 emissions.[5] In International Energy Agency's pathway to net zero, almost 90% of global electricity generation in 2050 should come from renewable sources, with solar PV and wind together accounting for nearly 70%.[6]

Solution-processed solar cells

Solar photovoltaics (PVs) are semiconductor devices that convert solar light into electricity directly. The vast majority of today's solar cells are based on silicon (first generation PVs), offering both reasonable prices and good power conversion efficiency. These cells are usually assembled into larger modules that can be installed on the roofs of residential or commercial buildings or deployed on ground-mounted racks to create huge, utility-scale systems.[7–9] Currently, the cell cost of silicon solar cells has declined rigorously. However, due to the low absorption coefficients of silicon, silicon are required to be thicker than hundred micrometers to gain adequate absorption in order to have high power conversion efficiencies. This prerequisite further limits silicon PV in various novel applications, such as semitransparent solar cells, building-integrated photovoltaics (BIPV) and automobile integrated photovoltaics, etc.

Another commonly used photovoltaic technology is known as thin-film solar cells (second generation PVs), which uses different materials such as cadmium telluride (CdTe) or copper indium gallium diselenide (CIGS).[10–12] The thickness of these cell layers is only a few micrometers. Thin-film solar cells can be flexible and lightweight, making them ideal for portable applications or for use in other products like windows that generate electricity from the sun. Some types of thin-film solar cells also benefit from manufacturing techniques that require less energy and are easier to scale-up than the manufacturing techniques required by their silicon counterparts.

Recently, solution-processed solar cells emerged as the third generation PV technologies, including perovskite solar cells, organic solar cells and nanocrystal solar cells.[13–18] The certified efficiency for emerging solar cells has been progressing incredibly fast, with the perovskite currently holding an efficiency record of 25.7% after only ten years' development,[19] which took silicon solar cells over 40 years to reach (Fig. 1.3). However, the scalability, stability and toxicity are still the main concerns for these materials.

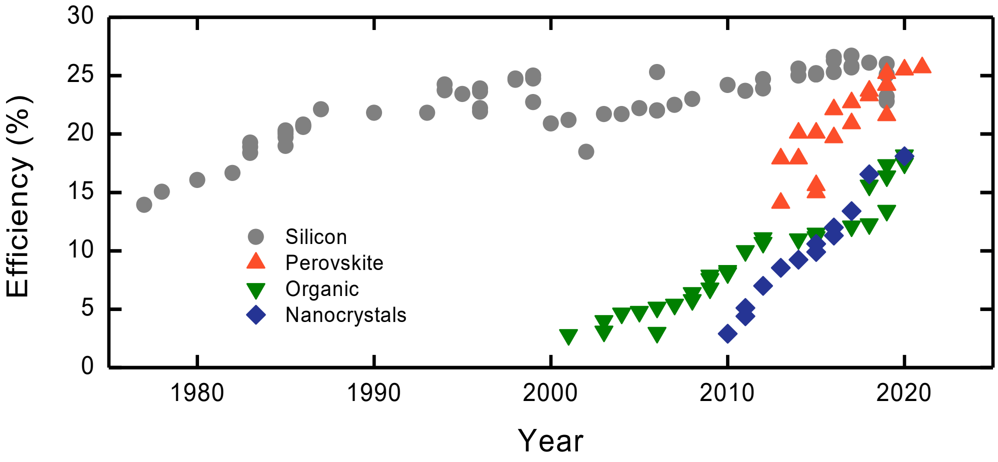

Figure 1.3 Best research-cell efficiency chart of various emerging solar materials and silicon cells.

Colloidal nanocrystal solar cells

Among the third generation solar cells, nanocrystal solar cells are one of the most promising technologies. Nanocrystals are crystalline particles as small as a few nanometers. As the surface-to-volume ratio increases rapidly with physical size decrease to nanometers, the surfaces of nanocrystals play an important role in their physical properties and applications.[20] Semiconductor nanocrystals can also have quantum confinement effects, provided the size is smaller than the excitonic bohr radius. [21]

Semiconductor nanocrystals can be synthesized with wet chemical processes from low-cost precursors.[22] The formation of high quality colloidal nanocrystals involves mainly two steps: a swift yet abundant nucleation and a controllable growth process.[22] The trophy for nanocrystal synthesis is narrow size-distribution, high yield and precisely controlled nanocrystal size. Size and monodispersity are also vital factors to the performance of nanocrystal based optoelectronic devices.

Only after obtaining high-quality nanocrystals, are people able to understand the fascinating properties of those tiny nanoscale materials. With quantum confinement effect, the absorption/photoluminescence and optical bandgap can be straightforwardly tuned by synthesizing different sizes.[23,24] With the modification of surface ligands, the nanocrystals showed different dispersity in polar/nonpolar solvents, enabling novel bio-imaging techniques.[25,26] Since the discovery, colloidal nanocrystals have become one of the most tunable and versatile nanoscale materials. They have been integrated into various semiconductor/optoelectronic devices, including photodetectors, light emitting diodes, lasers, transistors, solar cells, etc.[21]

In last decade, nanocrystal solar cells are mainly based on lead chalcogenide quantum dots.[17,18,23,27–29] Thanks to their large excitonic bohr radius and maturing synthetic approaches, monodispersed, high-quality size-controlled lead chalcogenide quantum dots have been synthesized and implemented into high performance optoelectronic devices.

As-synthesized semiconductor nanocrystals are typically capped with long, insulating organic ligands, hindering efficient charge transport in electronic devices. Different ligand-exchange processes, namely solid-state ligand-exchange and solution-phase ligand-exchange, have been introduced to substitute long ligands with short ones for conductivity.[30,31]

In solid-state ligand-exchange process, long insulating ligands capped nanocrystals are first deposited onto substrates, and nanocrystal films are then immersed or fully covered with a solution containing short, conductive ligands. The short conductive ligands, sometimes with the help of solvents, strip away and replace the original insulating ligands. The nanocrystal films are further rinsed with solvents to remove excess ligands and impurities. Many different ligands have been implemented into this solid-state ligand-exchange process, including short organic thiols, amines, inorganic halide ions, chalcogenide ions, etc. This strategy generally is performed as depositing very thin layers with a layer-by-layer style to avoid microscale cracks from volume loss after ligand-exchange.[32]

Different from the process of solid-state ligand-exchange, solution-phase ligand-exchange happens between two immiscible solvent phases; hence, it is also named phase-transfer ligand-exchange.[29,33–35] The prerequisites for solvents are the solubility (of ligands and nanocrystals) and immiscibility. Typically, ligands are dissolved in polar solvents, such as dimethyformamide (DMF), Dimethyl sulfoxide (DMSO), while the nanocrystals are dispersed in nonpolar solvents, like hexane or octane. As the ligand-exchange happens at the interface of two immiscible phases, vigorous mixing is required to maximize the interface area and facilitate the ligand-exchange. Rather than in nonpolar solvents, ligand-exchanged nanocrystals are dispersed in polar solvents and stabilized by the repulsive electrostatic forces from surface charges of polar ligands.[20] This method provides stable nanocrystal inks and enables single-step deposition for thin films of from a few nanometers to micrometers thick.[36]

Apart from synthesis and ligand-exchange, device structure also plays an important role on the performance of nanocrystal solar cells. In early stage, nanocrystal solar cells are built with Schottky junction architecture, where the nanocrystals are stacked between two metallic electrodes: one being transparent, such as indium doped tin oxide, and the other being vacuum-deposited metals, such as Al, Ag or Au. The device operates on the work function difference between two electrodes. The best-performing Schottky devices are based on lead sulfide quantum dots and achieved an efficiency up to 5%.[37,38]

Recently, heterojunction devices are developed to extend built-in electric field and improve collection of photo-generated charges.[39–41] A heterojunction device generally has a heavily doped metal oxide layer serving as charge transporting layer, where nanocrystal films are built on. Due to the doping density difference between metal oxide and nanocrystals, the built-in electric field at metal oxide/nanocrystals interface functions as the dominant workhorse for charge separation. Furthermore, the metal oxide/nanocrystals interface is intentionally made near front surface where maximum amount of charge carriers generate, therefore, maximizing the extraction efficiency and device performance. Following the same motivation, a similar interface can be made at the backside to further improve performance, namely n-i-p or p-i-n junctions. This design has become the mainstream of nanocrystal solar cells and provides the highest power conversion efficiency of up to 15%, together with outstanding air stability and operational stability.[17,18,27,29,30,42]

In the last five years, lead perovskite nanocrystals also surged as high performance materials for solution-processed solar cells. The power conversion efficiency of perovskite nanocrystal solar cells has climbed up to 18%; however, they tend to be unstable in air or under light.[43–46]

Figures of merit in solar cells

Solar cells convert illumination light into electricity directly. The solar cells generally are consisted of one electron-transporting (hole-blocking) layer (ETL), one photoactive absorber layer and one hole-transporting (electron-blocking) layer (HTL) for high-performance devices. The photoactive layer absorbs light and forms photo-generated charges, which are then separated by built-in electrical field and collected by transporting layers/electrodes.

The most important figure of merit for a photovoltaic device is the power conversion efficiency (PCE, η), which is power ratio of the maximum electrical output to the incident light. The power conversion efficiency is generally measured from a current-voltage sweep under illumination of a simulated solar light. The total light power of the simulated solar light is set to 100 mW/cm^2, which is the standard Air Mass 1.5 global (AM1.5G) solar light intensity. As shown in Fig. 1.4, taking into account of the device area, the current-voltage curve can provide information including the efficiency, short-circuit current density (J_{sc}) and open circuit voltage (V_{oc}). The short-circuit current density is the stable current density at zero bias under solar light illumination and the open circuit voltage is the bias where the current vanishes. The electrical output power can be computed as $P = J{*}V$ and the power conversion efficiency is the P_{max} divided by the total incident light power, 100 mW/cm^2. Another important parameter is the fill factor (FF), which can be calculated as:

$$FF = \frac{\eta}{J_{sc}V_{oc}}$$

FF generally includes the information about series resistance and shunt resistance: the lower series resistance and higher shunt resistance, the higher the fill factor.

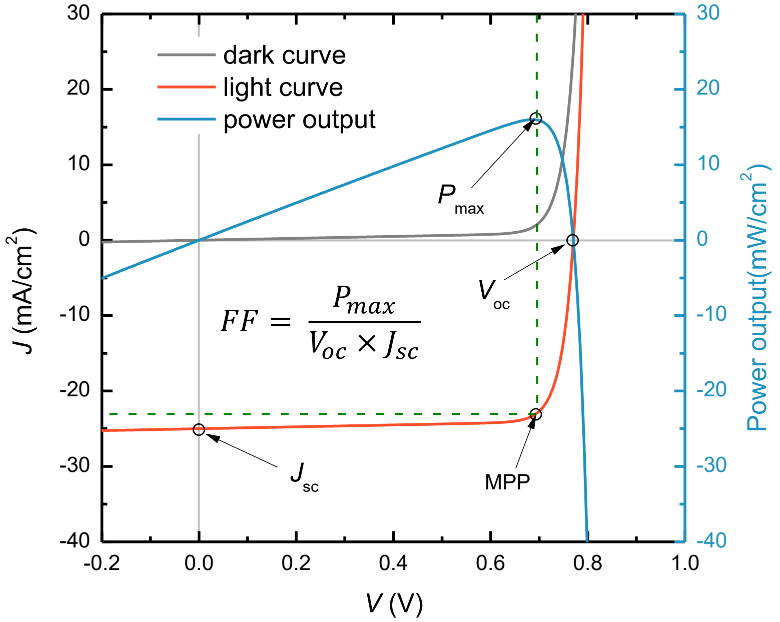

Figure 1.4 Typical current density-voltage (J-V) curve of a solar cell under dark and light illumination. *MPP, maximum power point.*

The short circuit current density can be determined not only from *JV* curve under illumination, but also from integrating external quantum efficiency. The external quantum efficiency (EQE) is the conversion quantum efficiency under monochrome light: the number ratio of output electrons to the input photons.

$AgBiS_2$ nanocrystal solar cells

Although lead based materials are providing high performance photovoltaic devices, as it is known, lead (Pb) is a highly toxic element.[47] Lead accumulates in the body and interferes with various biological processes, resulting in neurotoxic effects with a series of symptoms. Long-term exposure of Pb can lead to severe brain damage and kidney dysfunctional. Lead is also included in the Restriction of Hazardous Substances Directive (RoHS) in Europe, preventing Pb based devices entering the consumer electronics.

In order to eliminate lead, many efforts have been paid to substitute lead with other low-toxic or non-toxic elements, such as antimony, copper, tin, indium, silver and bismuth, etc., leading to a plethora of non-toxic materials studies.[48–54] Among numerous non-toxic photovoltaic materials, few of them meets all the four most important properties: efficiency, stability, processibility and non-toxicity (Fig. 1.5). Antimony (Sb) chalcogenide and Coper-Zinc-Indium-Sulfide/selenide (CZTS) have surpassed 10% efficiency recently, however, they require cadmium sulfide (CdS) as interface layers or high temperature annealing for crystallization. As an opposite, dye sensitized solar cells (DSSC) based on $CuInSe_2$ quantum dots perform without toxic layers or high temperature processes, but they suffer from unstable liquid electrolytes. Tin perovskite has been developed in last few years, following the rise of lead halide perovskites. Although record performance up to 15% has been reported, the intrinsically unstable Sn^{2+} in air still severely affects the device stability.

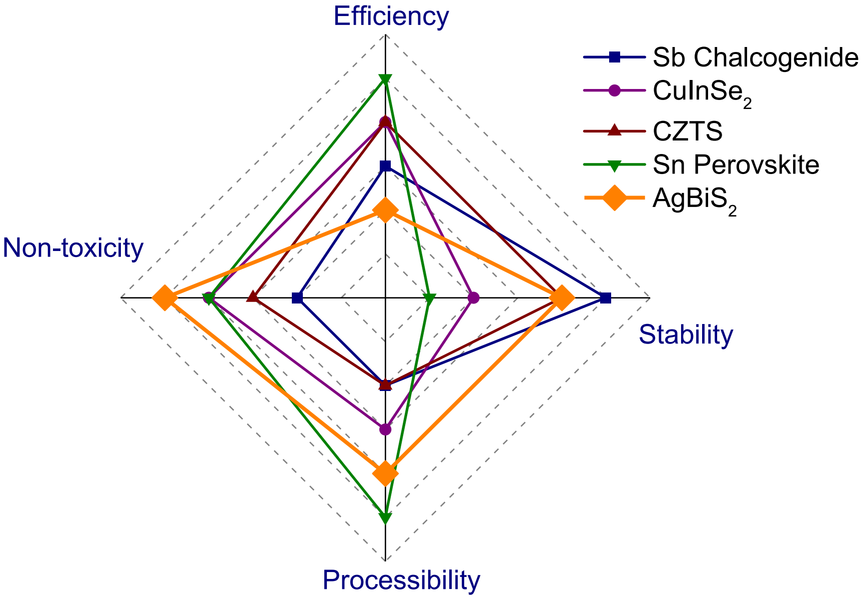

Figure 1.5 Comparison of most important properties of environmentally friendly solar materials.

Silver bismuth sulfide nanocrystals are one of the most promising photovoltaic materials with solution-processibility, high-stability and high absorption coefficients. In its nanocrystalline form, $AgBiS_2$ exhibits photoconductivity and favorable thermoelectric properties and has been used as a sensitizer or counter-electrode in sensitized solar cells with modest efficiencies.[55–57]

In 2016, our group has demonstrated the synthesis of high quality $AgBiS_2$ nanocrystals and a solution-processed colloidal nanocrystal solar cell with power conversion efficiency up to 6.3% (Fig. 1.6),[58] which was the first efficient inorganic solar material that simultaneously meets the demands for non-toxicity, abundance and low-temperature processing.

However, the device performance was limited by poor charge carrier transport. The short-circuit current density under one sun illumination decreased when using thicker absorber films. Poor carrier transport and Shockley–Read–Hall (SRH) trap-assisted recombination were responsible for incomplete charge extraction before recombination.[58,59]

Although many attempts have been done to improve the surface passivation for better charge carrier transport and thus higher device performance, the power conversion efficiency of $AgBiS_2$ nanocrystal solar cells have been stagnating at ~6% for over five years.[59–62] New approaches are urged to further improve the device performance and make $AgBiS_2$ nanocrystal solar cells more competitive to other materials.

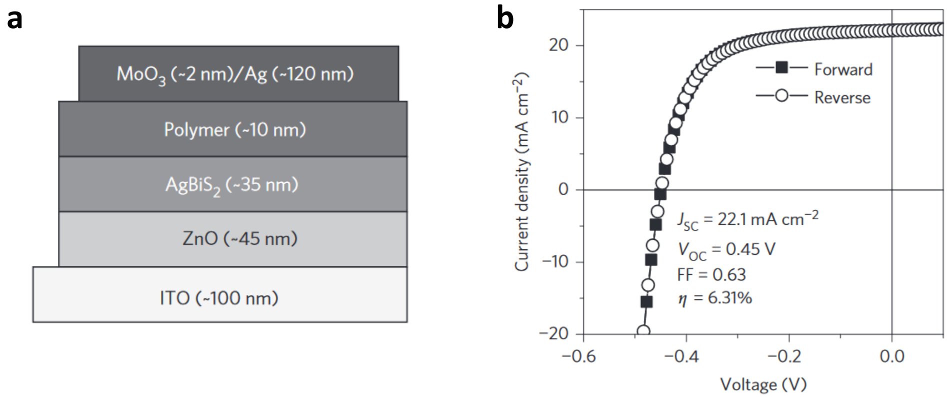

Figure 1.6 First demonstration of 6.3% efficiency $AgBiS_2$ nanocrystal solar cells in 2016. *a, structure of $AgBiS_2$ solar cell. b, JV curve of certified $AgBiS_2$ solar cell. Figure adapted from ref*[58]*, copyright by Nature Publishing Group.*

Thesis Outline

$AgBiS_2$ nanocrystals are extremely promising for solution-processed inorganic solar cells, for their non-toxic, earth-abundant and highly absorbing nature. This thesis is focused on investigating the atomic arrangements and material processing to improve the device performance and meet the manufacturing prerequisites. More specifically the following issues are addressed in this work:

Enhancement of optical absorption: the optical absorption of a semiconductor has been seen as an intrinsic property and can only be enhanced by optical means. In Chapter 2, we leverage the fundamental relation between atomic arrangements and transition probability to improve the absorption in ultrathin nanocrystal films. We found the absorption coefficients of ternary $AgBiS_2$ nanocrystals can be enhanced via cation-disorder homogenization under mild annealing. An absorption coefficient higher than any other currently used photovoltaic materials is obtained. The transition in cation configuration is also confirmed by the combination of ab initio calculations and experimental techniques.

Efficient ultrathin solar cells: High-performance, lightweight ultrathin solar cells have been a long-sought target in the photovoltaic field for their reduced material consumption and manufacturing demands. In Chapter 3, we first estimate a spectrum limited maximum efficiency (SLME) of over 26% for a 30 nm nanocrystal film with transfer matrix method (TMM). Ultrathin solar cells are further fabricated based on the ultra-absorbing $AgBiS_2$ nanocrystals. A high J_{sc} of 27 mA cm^{-2} and a record efficiency of up to 9.17% were obtained with an independent certification of 8.85% from Newport, USA. The air stability and photostability were also recorded in high-performance devices.

Eco-friendly nanocrystal inks: As a commercial product, solar cells have to be massive-manufacturable. Current layer-by-layer depositing process are time and material-consuming. In Chapter 4, we developed a method for completely environmentally friendly $AgBiS_2$ nanocrystal inks via solution-phase ligand-exchange. 3-mercaptopropionic acid and methanol are chosen as ligand and solvent pair for fast ligand-exchange with oleic acid capped nanocrystals. Benefiting from the water based $AgBiS_2$ nanocrystal ink, fully green-processed photovoltaic devices are fabricated. A power conversion efficiency up to 7.3% was achieved with superior air stability. Device characterizations were conducted and we pointed out that current devices are limited by trap-assisted recombination in absorber layer.

Chapter 2 Enhanced optical absorption via cation-disorder homogenization

This chapter is based on the following publication:

Cation-disorder Engineering Yields $AgBiS_2$ Nanocrystals with Enhanced Optical Absorption for Efficient Ultrathin Solar Cells. *Nat. Photon.* 2022, 16 (3), 235–241.

Optical absorption and cation-disorder

The absorption coefficient of a semiconductor has been considered as a fundamental parameter of the material, with efforts to enhance ligand absorption in ultrathin absorbers relying on optical means. [63,64]

In this chapter, we instead start from the fundamental relationship between atomic geometry, electronic structure and optical absorption. We propose that the absorption coefficient of a semiconductor can be tuned by engineering the atomistic material structure.

In crystalline semiconductors, the valence electrons of each atom overlap and hybridize into band structures. The optical absorption can be computed from local density of states according to Fermi's Golden Rule.

$$Transition\ Probability \propto \int_{BZ} \left|\vec{\epsilon} * \boldsymbol{\mu}_{if}\right|^2 \rho_{if}(E)\, \delta\left(\Delta E - E_{ph}\right) dE$$

Where ρ_{if} is the joint density of states between initial states and final states, and $\left|\vec{\epsilon} * \boldsymbol{\mu}_{if}\right|^2$ is the transition dipole moment matrix element, which is highly correlated with the overlap between the wave-functions of initial and final states. Hence, theoretically, by manipulating the overlap between wave-functions, the optical absorption can be enhanced in the atomic level.

Cation-disorder is a widely observed phenomenon in multinary materials, referring to the deviation of atomic positions in the cationic sub-lattice from an ordered crystalline arrangement. This phenomenon substantially impacts in the optoelectronic properties of semiconductors and has traditionally been considered an undesired and often unavoidable effect, due to its entropically driven nature.[65–68] We leverage the modulation of cation-disorder homogeneity in multi-nary semiconductors as a pathway to enhance the optical transition matrix elements such that improved absorption coefficient and higher absorption in ultrathin absorbers.

Cation-disorder dependent band structure

Silver bismuth sulfide ($AgBiS_2$) nanocrystals is a solution-processed nanomaterial comprising environmentally friendly elements with reported efficiency exceeding 6% in thin film solar cells.[58] The cation distribution around Ag sites in $AgBiS_2$ NCs has shown evidence for non-random Ag–Ag correlation, indicating the presence of inhomogeneous cation-disorder (that is, cation segregation with local Ag-rich and Bi-rich regions), likely due to growth kinetics during synthesis and surface–ligand interactions.[69]

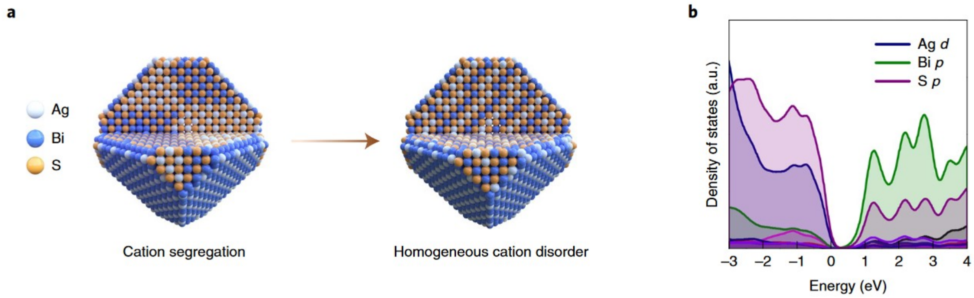

Figure 2.1 ***Cation-disorder and homogenization in*** $AgBiS_2$***.*** *a, Schematic of* $AgBiS_2$ *NCs with cation segregation and homogeneous cation-disorder configuration. b, Electronic density of states of homogeneous disordered* $AgBiS_2$*. The VBM is set to 0 eV.*

An illustration of inhomogeneous cation-disorder within $AgBiS_2$ NCs is shown in Fig. 2.1a. The valence band maximum (VBM) of $AgBiS_2$ primarily derives from Ag d and S p states, whereas the conduction band minimum (CBM) arises from Bi p and S p interactions (Fig. 2.1b).

A clear spatial separation of the Ag-derived VBM and Bi-derived CBM for the cation-segregated configuration can be observed in the local electronic density of states (Fig. 2.2a). In contrast, under homogeneous cation-disorder, we predict a VBM and CBM delocalized over the entire material (Fig. 2.2b), with the correlation between cation distribution and spatial (de)localization of the band extrema (Fig. 2.2c).

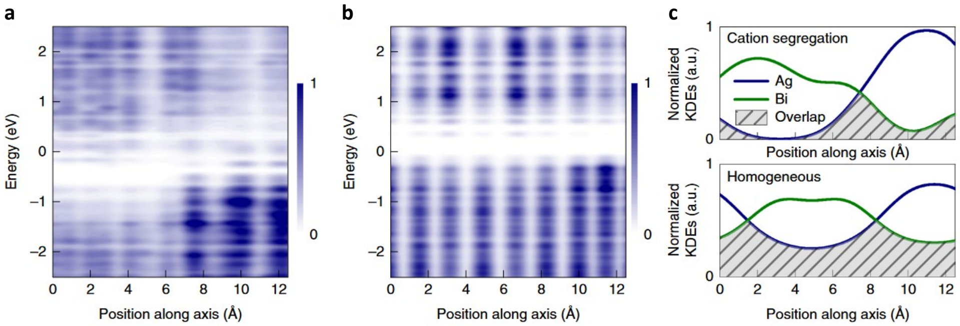

Figure 2.2 Electronic density of states of $AgBiS_2$ with different cation distributions. *a, Planar-averaged local electronic density of states for (a) cation-segregated $AgBiS_2$ and (b) homogeneous cation-disordered $AgBiS_2$. The colour bar indicates normalized$\sqrt{\boldsymbol{DOS}}$. c, Normalized kernel density estimates (KDEs) of Ag and Bi for cation segregation and homogeneous cation-disordered $AgBiS_2$. The shadow area shows the overlap of Ag and Bi KDEs.*

Cation-disorder homogeneity and absorption behavior

The theoretically simulated optical spectra of $AgBiS_2$ for both inhomogeneous and homogeneous cation-disorders are provided in Fig. 2.3. As expected, we find a substantially increased refractive index *n* and transition dipole matrix element and therefore enhanced optical absorption on homogenizing disorder.

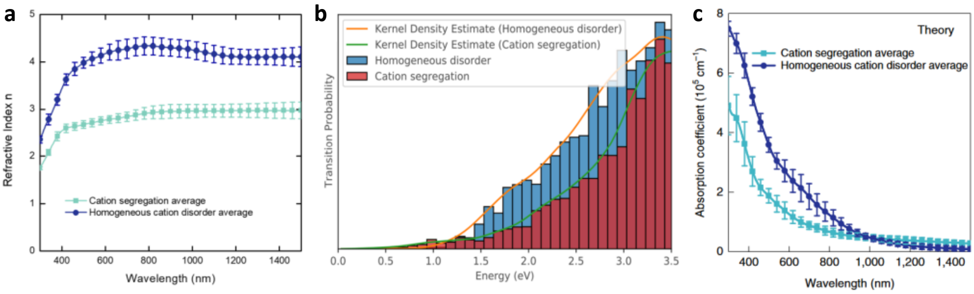

Figure 2.3 Simulated optical properties of $AgBiS_2$ with different cation distributions. *a, Simulated refractive index n for cation segregation and homogeneous disorder cases. b, Electronic transition probabilities for segregated and homogeneous cation distributions in $AgBiS_2$. Shown as a histogram plot with bin widths of 0.1 eV, alongside Gaussian Kernel Density Estimate (KDE) fit lines. c, Simulated absorption coefficients of $AgBiS_2$ with different cation distributions. The data are presented as mean values ± standard deviation.*

To experimentally tune the cationic disorder, we first assessed the thermodynamics of atomic reordering, particularly the formation energy difference needed to induce disorder. Density functional theory (DFT) was employed to calculate the inter-site cation exchange energy. Under the highest level of theory employed for phase energetics (hybrid DFT including spin–orbit-coupling effects), the bulk order–disorder enthalpy difference is calculated as 17.4 meV per atom, indicating the accessibility of cation site swapping in $AgBiS_2$ under mild annealing conditions. The mechanism behind cation inter-site exchange probably is defect-mediated ionic migration. Indeed, cation mobility aided by Ag vacancies and bond anharmonicity has been demonstrated in $AgBiS_2$ NCs.[70–72]

Considering the low inter-site cation exchange energy in $AgBiS_2$, we sought to anneal $AgBiS_2$ NCs under low-temperature conditions to facilitate cation inter-site exchange and thus an entropically driven transition to homogeneous cation distribution. Fig. 2.4a plots the absorption coefficient of our NC films on annealing under different temperatures. Comparing Fig. 2.3c and Fig. 2.4a, the simulated absorption spectrum for cation segregation configurations (inhomogeneous disorder) matches well with the as-prepared $AgBiS_2$ NC film, both exhibiting Urbach band tailing at longer wavelengths, which is pernicious for photovoltaic devices.[29,73] However, in the homogeneous cation-disordered structure, the simulated absorption coefficient is much higher than the cation-segregated case, with reduced band tailing, manifesting favorable properties for optoelectronic applications.[74] As shown in Fig. 2.4a, the absorption coefficient of $AgBiS_2$ NC films is enhanced by up to a factor of two after annealing, alongside reduced Urbach energy from 173 to 26 meV (Fig. 2.4b), as predicted by ab initio calculations.

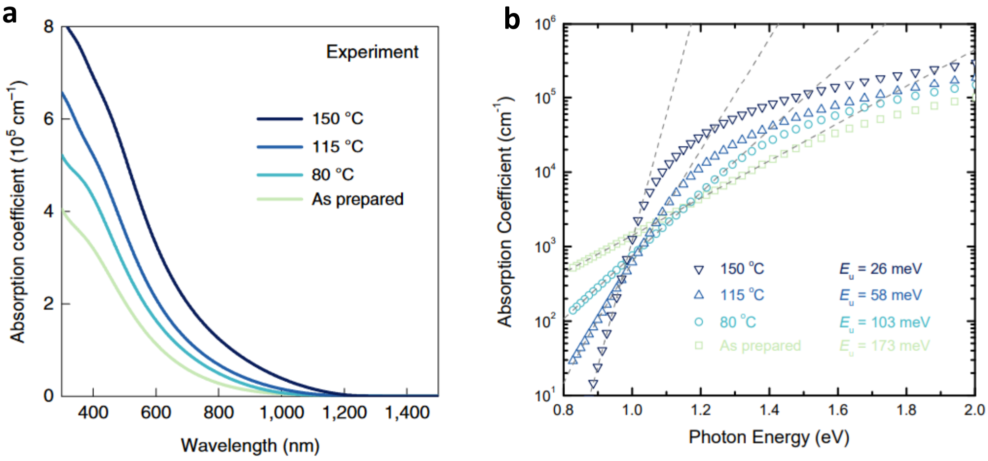

Figure 2.4 Absorption coefficients of $AgBiS_2$ NC films before and after annealing. *a, Absorption coefficients and, b, Urbach tails of $AgBiS_2$ NCs annealed at different temperatures. The Urbach energy for as-prepared, 80°C, 115°C and 150°C annealed films are 173meV, 103meV, 58meV and 26meV, respectively. For all fittings, the coefficient of determination R^2 is greater than 0.995.*

Furthermore, this enhanced absorption is stable in the ambient atmosphere, as spontaneous cation segregation is thermodynamically and entropically unfavorable (Fig. 2.5). The reflectance and transmittance of as-prepared and annealed films are monitored for a period of 17 days, while no obvious spectrum change can be observed.

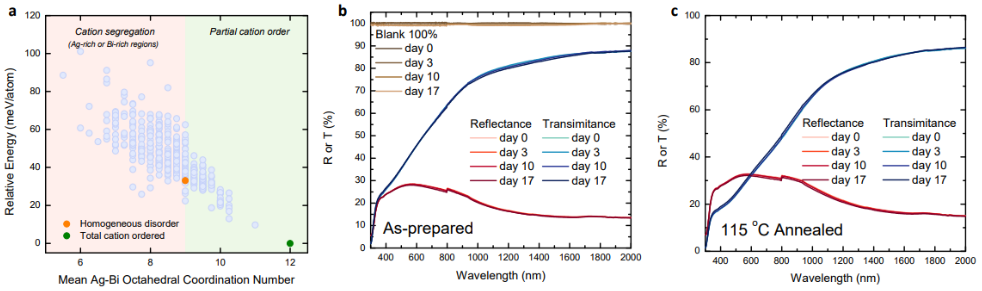

__Figure 2.5 Stability of enhanced absorption coefficient via cation-disorder homogenization.__ a, Relative energy vs mean Ag-Bi octahedral coordination number for various cation configurations in $AgBiS_2$. Energy given relative to total cation ordered configuration. b, and c, Reflection and transmission of as-prepared and 115°C annealed $AgBiS_2$ NC film on glass substrates.

With this low-energy, scalable annealing process, we produce a semiconducting material that exhibits an absorption coefficient 5–10 times greater than any other material currently used in photovoltaic technology,[11,64,75–78] across a wide spectral range from 400 to 1,000 nm (Fig. 2.6).

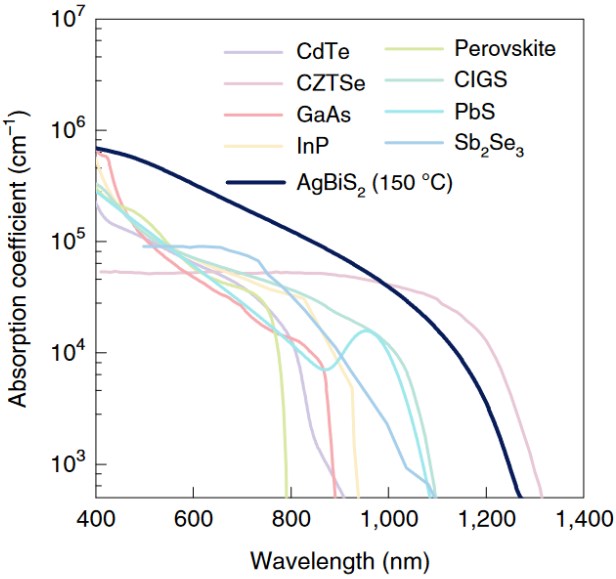

Figure 2.6 Absorption coefficient of $AgBiS_2$ NC films compared with other photovoltaic materials. *CdTe (ref.[11]), CZTSe (ref.[75]), GaAs (ref.[64]), InP (ref.[76]), perovskite,[77] copper indium gallium selenide (CIGS),[64] PbS and Sb_2Se_3 (ref.[78]).*

Cation configuration transition

To further verify the proposed cation homogenization as the underlying mechanism responsible for the optical absorption enhancement in $AgBiS_2$ NC films, film thicknesses were first measured to exclude NC densification as the dominant factor. Negligible thickness changes were observed between the as-prepared and the samples annealed at 115 °C (Fig. 2.7), with only a slight decrease for the films annealed at 150 °C, contributing to a very small (~8%)

absorption enhancement for this sample. These film thickness measurements demonstrate that the densification effect is not the dominant factor in the absorption enhancement of these materials.

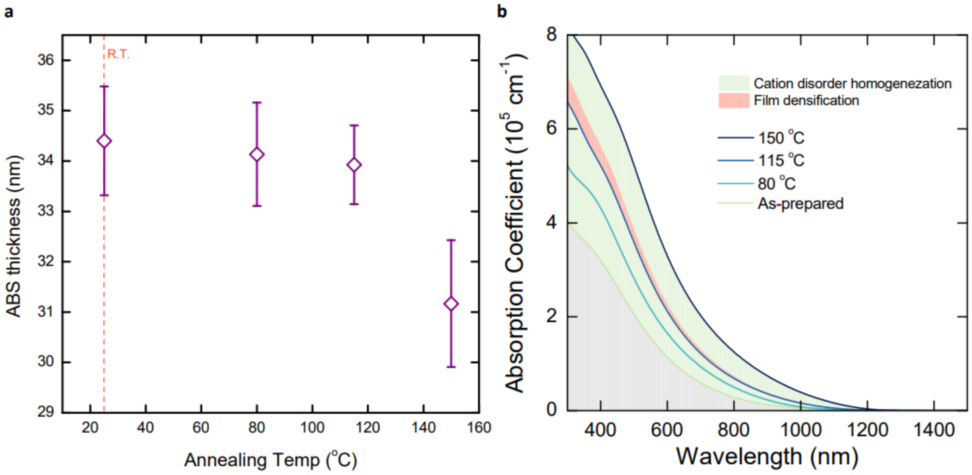

Figure 2.7 Contribution of absorption coefficient enhancement from film densification. *a, Thickness measurements of* $AgBiS_2$ *NC films annealed at different temperature. Data are presented as mean values ± standard deviations. b, Contribution of cation-disorder homogenization and film densification to absorption coefficient enhancement.*

Furthermore, we used X-ray diffraction (XRD) and transmission electron microscopy (TEM) to probe the changes in the crystal structure due to cation-disorder homogenization on annealing. Interestingly, although XRD analysis suggested increased crystallite size (from 4.2 to 6.2 nm) on annealing at

115 °C, high-resolution transmission electron microscopy (HRTEM) showed no measurable size differences in these samples (Fig. 2.8a &b). The sharpening of the XRD peaks despite negligible NC growth indicates improved crystallinity due to atomic rearrangements within the NCs.

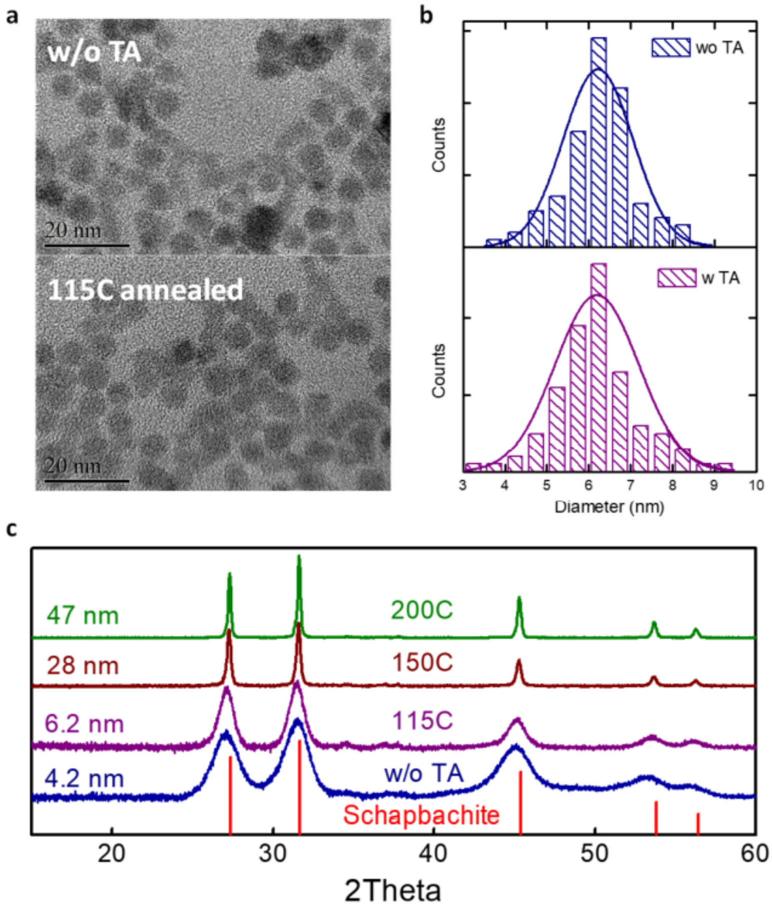

Figure 2.8 AgBiS$_2$ NCs size characterization. *a, TEM images and, b, size distributions of AgBiS$_2$ NCs before and after 115 ℃ annealing. The size distribution from TEM images are 6.2 ± 0.8nm and 6.2 ± 1.0 nm. c,*

Experimental XRD patterns of $AgBiS_2$ NCs annealed at different temperatures. The XRD size was extracted by fitting the experimental XRD pattern with the ideal Schapbachite structure.

Further increasing the annealing temperature to 150 and 200 °C causes the NCs to fuse into larger crystals (28 and 47 nm, respectively; Fig. 2.8c). Point defects are observable in the HRTEM data after high-temperature annealing, which could be harmful for optoelectronic applications (Fig. 2.9).[79]

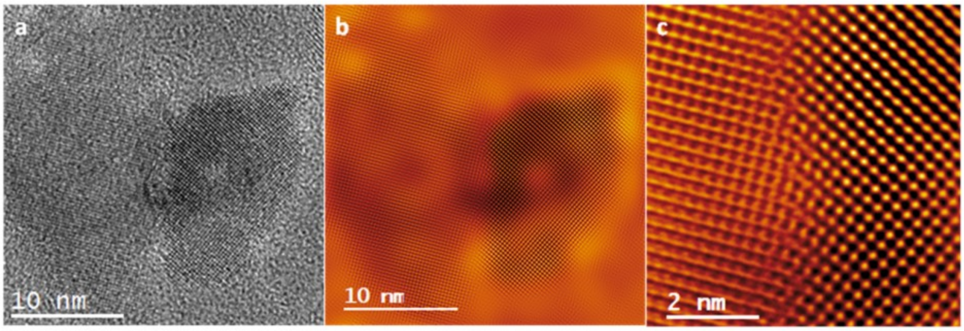

Figure 2.9 HRTEM images of $AgBiS_2$ NCs annealed at 200℃. *a, HRTEM image showing two $AgBiS_2$ NCs fusing together. b, Inverse FFT image of a, for higher resolution. c, Zoom in of the nanocrystals boundary showing defects present. Point defects can be seen in b and c, due to uncontrolled nanocrystals fusing.*

In addition to peak narrowing in the XRD patterns, the peak positions were also found to shift to higher angles on annealing (Fig. 2.10).

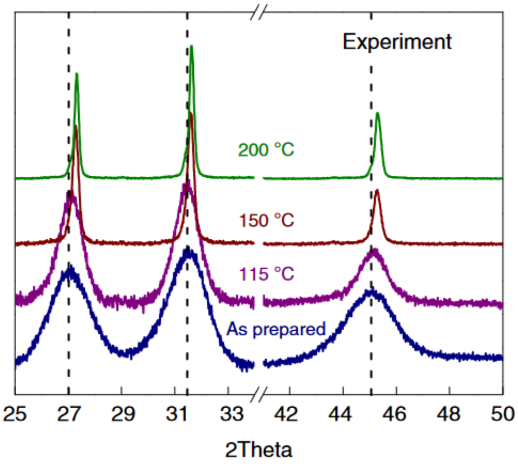

Figure 2.10 Experimental XRD patterns of $AgBiS_2$ NCs annealed at different temperatures.

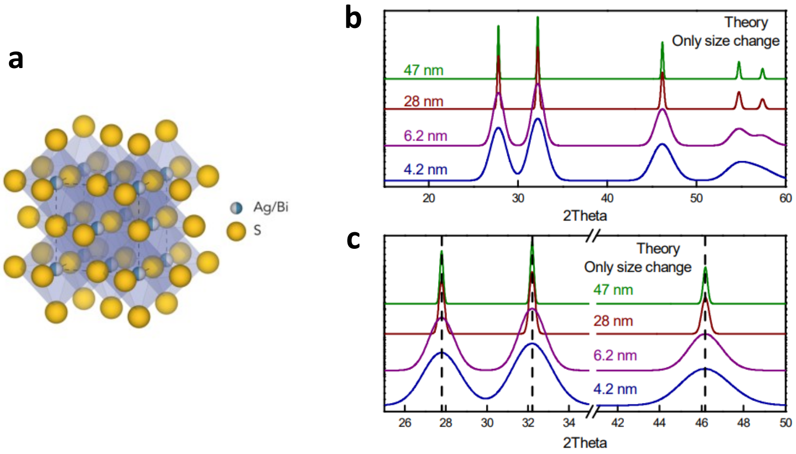

Figure 2.11 Crystal structure and simulated XRD patterns of $AgBiS_2$ NCs.

a, Schematic of Fm3m cubic $AgBiS_2$. b, &c, Simulated XRD patterns of *homogeneous-disorder $AgBiS_2$ with nanocrystal size as the only variable. Uniform peak sharpening is observed with nanocrystal growth, with no movement of the peak positions. Dashed lines are a guide to the eye.*

To deconvolute the effect of crystal size and cation arrangement, as well as explain the apparent changes in crystallinity, we calculated the expected XRD patterns for homogeneously disordered cubic $AgBiS_2$ (space group $Fm\bar{3}m$; Fig. 2.11a), with crystal size as the only variable parameter (Fig. 2.11 b&c). The full-width at half-maximum of all the peaks sharpens with crystal growth, whereas the peak positions remain essentially the same, as expected.

However, when transitioning from cation-segregated configurations to homogeneous cation-disorder, as well as fixing the crystallite size, the simulated XRD patterns of $AgBiS_2$ show distinct peak shifts to higher angles and peak narrowing (Fig. 2.12a), matching the experimental observations of improved crystallinity on annealing. These XRD peak shifts primarily originate from the shortening of the Ag–S bond lengths, whereas peak narrowing occurs due to narrowing of the bond length distributions and reduction in octahedral distortion on homogenization of the cation distribution (Fig. 2.12b).

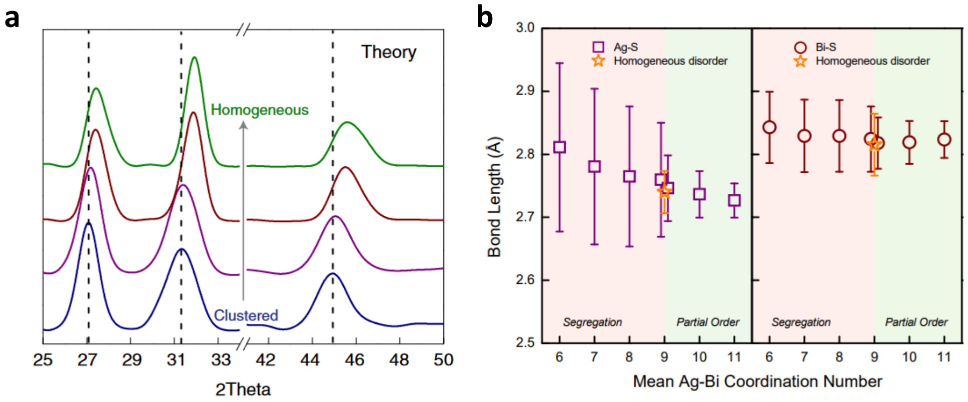

Figure 2.12 Simulated crystal structure of $AgBiS_2$ with different cation distributions. *a, Simulated XRD of 10 nm $AgBiS_2$ NCs with varying cation distribution homogeneities, from cation segregation to homogeneous cation-disorder. b, Bond length dependence on cation order/disorder in $AgBiS_2$. Average cation-anion bond length for various cation configurations in $AgBiS_2$. The average Ag-S bond length decreases and the range narrows with cation homogenisation. The average Bi-S bond length follows the same trend, but to a lesser extent.*

Since the XRD peak shift correlates with the inter-plane distance in $AgBiS_2$ crystals, this phenomenon was further confirmed with HRTEM measurements (Fig. 2.13), with integrated line profiles of the {200} plane showing a slight shrinkage after annealing, further confirming the transition from cation segregation to homogeneous disorder.

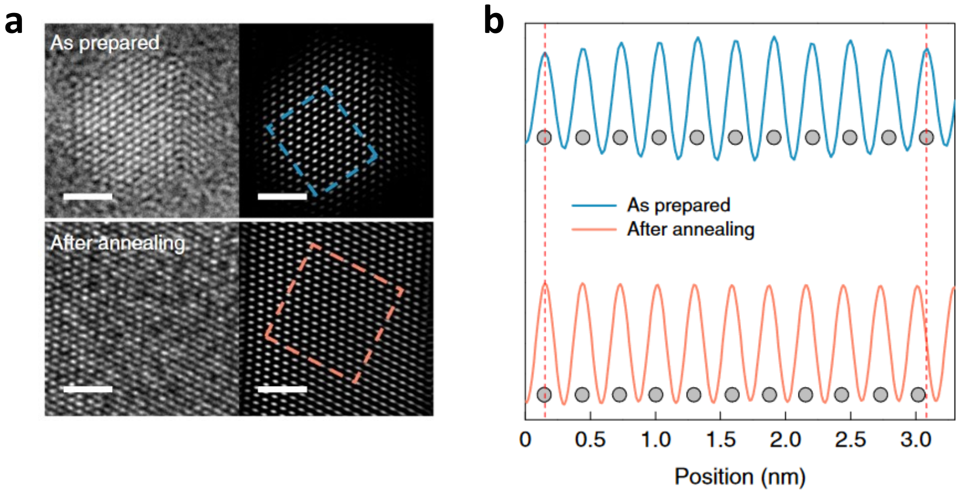

Figure 2.13 High-resolution transmission electron microscope (HRTEM) Characterization. *a, HRTEM images of $AgBiS_2$ NCs before and after annealing at 200 °C. Scale bar, 2 nm. b, Integrated line profiles of the {200} crystal plane indicated by the dashed lines in a.*

Apart from the crystal structure transformation, changes in the Madelung potential were also expected, considering the difference in local bonding environments for different cation configurations.[80] Hence, we calculate the average Madelung potential at the Bi sites as 3.29 and 4.66 V for segregated and homogeneous cation configurations, respectively, using Bader atomic charges. A greater Madelung potential suggests a decrease in the X-ray photoelectron (XPS) binding energy, on transitioning from inhomogeneous to homogeneous cation-disorder.[80,81] As shown in Fig. 3e, the Bi 5d peaks in the simulated XPS spectra are noticeably shifted to lower binding energies for homogeneous cation-disorder, compared with cation-segregated configurations. Likewise, the annealed $AgBiS_2$ NCs show a small but notable chemical shift to a lower energy, compared with the as-prepared samples (Fig. 2.14), in agreement with our proposition of cation homogenization on annealing.

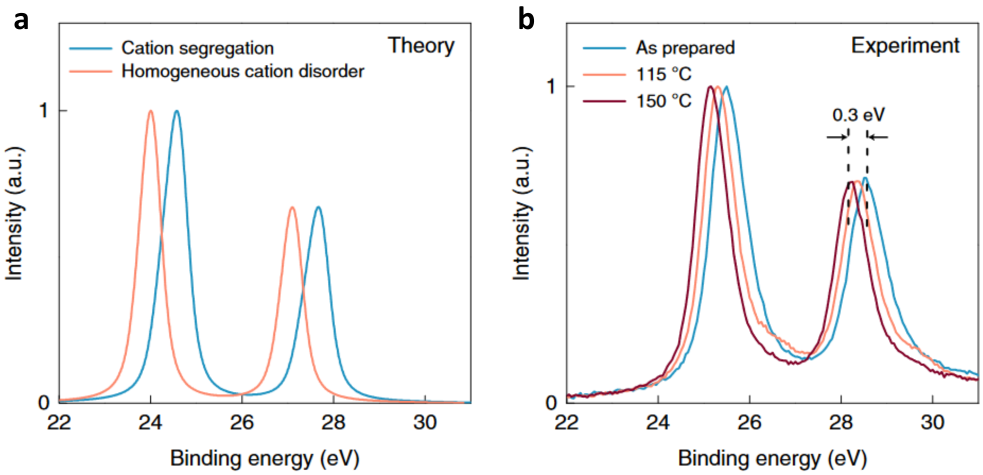

Figure 2.14 Chemical environment characterization of $AgBiS_2$ with different cation distributions. *a, Simulated valence-band XPS spectra of* $AgBiS_2$ *with different cation configurations. b, Experimental XPS spectra of* $AgBiS_2$ *NCs annealed at different temperatures. The dashed lines indicate the peak positions before and after annealing.*

Summary

In conclusion, we have demonstrated that the absorption coefficient of ternary $AgBiS_2$ NCs can be enhanced via cation-disorder homogenization under mild annealing conditions. Ultrahigh absorption coefficients were obtained in annealed $AgBiS_2$ NC films. The transition in cation configuration was further confirmed by the combination of ab initio calculations with XRD, HRTEM and XPS measurements. This chapter not only demonstrates an ultra-absorbing nanocrystal material, but also demonstrates the importance of atomic configuration engineering in multinary systems.

Chapter 3 Ultrathin solar cells based on $AgBiS_2$ nanocrystals

This chapter is based on the following publication:

Cation-disorder Engineering Yields $AgBiS_2$ Nanocrystals with Enhanced Optical Absorption for Efficient Ultrathin Solar Cells. *Nat. Photon.* 2022, 16 (3), 235–241.

Introduction to ultrathin solar cells

High-performance, lightweight solar cells featuring low cost and environmental friendliness have been a long-sought target in the photovoltaic field. Ultrathin solar cells can reduce material consumption and manufacturing demands, directly lowering the cost. Owing to an absorber thickness that is orders of magnitude lower than conventional solar cells, ultrathin solar cells further allow for flexible and lightweight form factors suited for building- or wearable-integrated photovoltaics. A thinner absorber layer also improves charge carrier collection and reduces bulk recombination, which are particularly prevalent in nanocrystalline solution-processed semiconductors,[20,58] thus improving performance, provided strong light absorption. Furthermore, high absorption in small absorber volumes allows for operating the device at high photogenerated carrier densities, a physical regime that maximizes the open-circuit voltage (V_{oc}) and permits advanced high-efficiency concepts such as hot carrier solar cells.[82]

Currently, high-performance ultrathin solar cells are mainly realized via different light-trapping strategies, which are employed to compensate for the short-circuit current drop due to incomplete absorption in the ultrathin absorbing layer.[63,64] The use of optical architectures, however, increases non-radiative recombination and complicates the manufacturing process, introducing additional obstacles towards low-cost high-efficiency devices.[64,83]

Optical modelling

Typically, the absorption coefficient of a material determines the required thickness for optimal light harvesting under photovoltaic operation. With the high absorption coefficient of our films achieved in previous chapter, an ultrathin layer of $AgBiS_2$ NCs would be sufficient to absorb most of the light in the visible range. To assess the potential of our strongly absorbing NC films, we calculate the maximum achievable short-circuit current density J_{sc} using the transfer matrix method (TMM),[84,85] assuming 100% internal quantum efficiency (IQE) (Fig. 3.1). The stacks are assumed as the most commonly used device structure: Glass/ITO/ETL/Absorber/HTL/Ag. Considering the minor difference between different transporting layers, the refractive indices for ETL and HTL are assumed to be 2 with extinction coefficients of zero.

The wavelength dependent total light absorption in $AgBiS_2$ layer was first calculated with TMM with the input of optical constant data (Fig. 3.1) and was further considered as external quantum efficiency (EQE_{TMM}) of the corresponding device based on the assumption of 100% IQE. Short circuit current density was further calculated as:

$$J_{sc} = \int_{0}^{+\infty} EQE_{TMM} \times \emptyset_{AM1.5G}\, dE$$

Where $\emptyset_{AM1.5G}$ is the standard solar spectrum on the ground when the sun is at a zenith angle of 48.2°, with the intensity of 1000 $W{\cdot}m^{-2}$.

Fig.3.2a plots the maximum J_{sc} as a function of the active layer thickness for different annealing temperatures, corresponding to varying degrees of cation-disorder homogeneity. On increasing the annealing temperature, we witness an increase in J_{sc} at low active layer thicknesses ($t < 200$nm). We predict a maximum J_{sc} of ~28 mA cm^{-2} (or 32 mA cm^{-2}) for $AgBiS_2$ NC films annealed at 115 °C (or 150 °C), with a thickness of only ~30 nm.

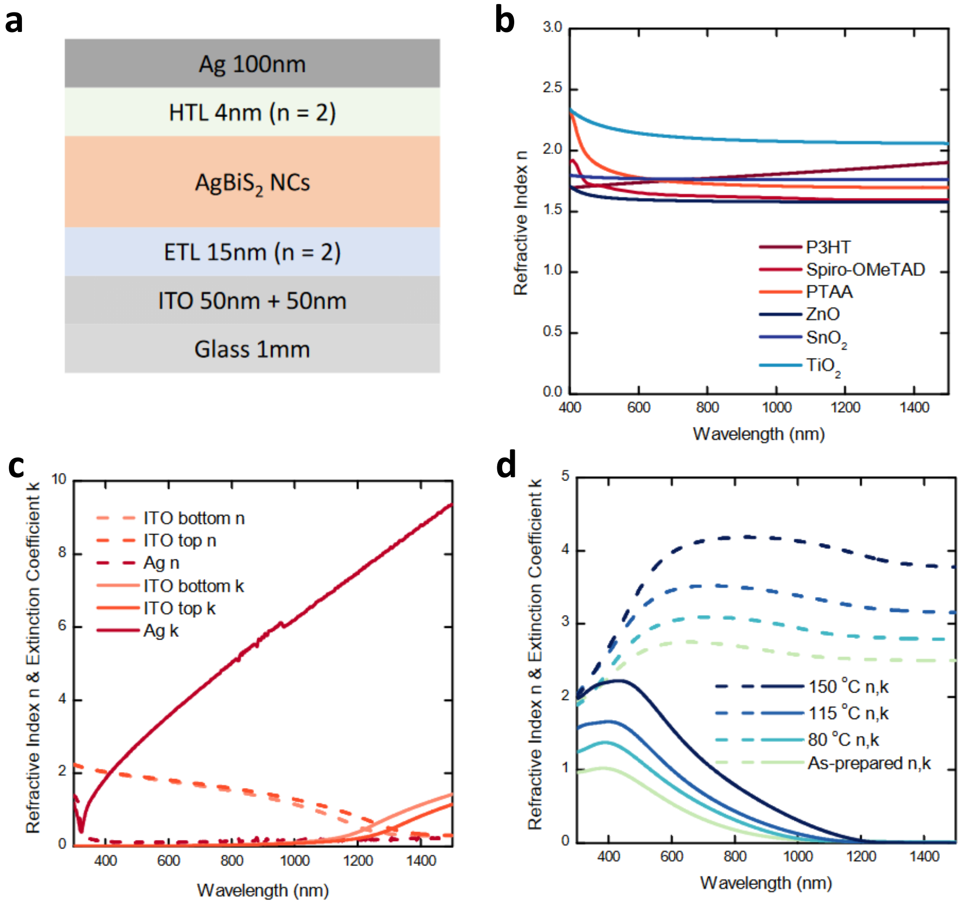

Figure 3.1 Optical modelling via the Transfer Matrix Method (TMM). *a, Device structure used for TMM calculations. b, Refractive indices n of commonly-used electron transport layers (ETLs) and hole transport layers (HTLs). c, Refractive indices n (dashed lines) and extinction coefficients κ (solid lines) of ITO and Ag electrodes. d, Refractive indices n (dashed lines) and extinction coefficients κ (solid lines) of* $AgBiS_2$ *NC films annealed at different temperatures. ITO layer was considered as two layers (50 nm top*

layer and 50 nm bottom layer) to mimic the vertical refractive index inhomogeneity.

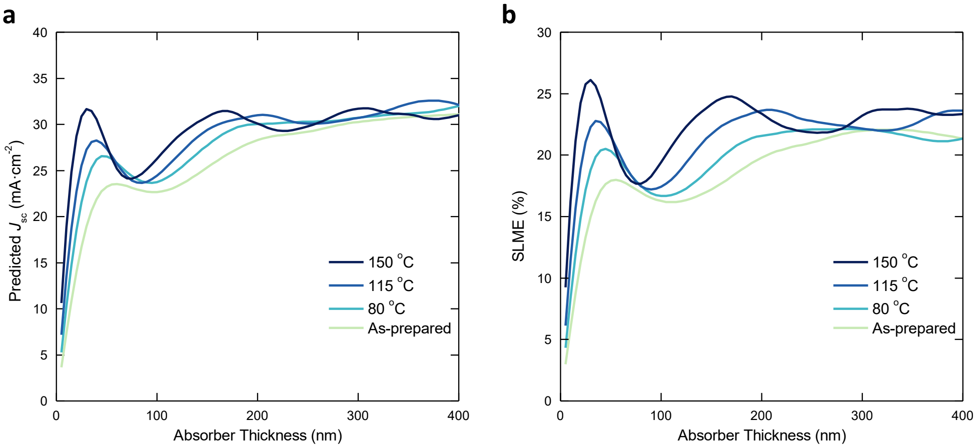

***Figure 3.2 Theoretical device performance predicted by TMM simulation.** a, Predicted short-circuit current density (J_{sc}) of $AgBiS_2$ NCs using the TMM. b, The SLME of $AgBiS_2$ NCs as a function of film thickness.*

Furthermore, the spectroscopic limited maximum efficiency (SLME) was calculated assuming only radiative recombination in the devices[86]:

$$SLME = P_{max}$$

$$P = -V \times \left\{ J_0 \left[\exp\left(\frac{eV}{kT}\right) - 1 \right] - J_{sc,TMM} \right\}$$

Where e denotes the elementary charge; k, the Boltzmann constant; T, the temperature; and J_0, the dark saturation current density calculated with the assumption of only radiative recombination:

$$J_0 = e \times \int_0^{+\infty} EQE_{TMM} \times \emptyset_{BB}(E)\, dE$$

Where $\emptyset_{BB}$ is the black-body radiation spectra at 300K.

As shown in Fig. 3.2b, a high photovoltaic efficiency up to 26% was predicted for a 30 nm absorber layer, indicating the performance potential of ultrathin solar cells based on $AgBiS_2$ NC films.

Hole transporting layers and device performance

Having developed a material with such strong optical absorption and high predicted-efficiency, we next sought to produce highly efficient ultrathin solution-processed solar cells with these NCs. The solar cells were fabricated with an architecture of glass/indium tin oxide (ITO)/SnO_2/$AgBiS_2$/ hole transport layer (HTL)/MoO_3/Ag (Fig. 3.3a). Cross-sectional TEM confirms the ultrathin nature of the device layers (Fig. 3.3b).

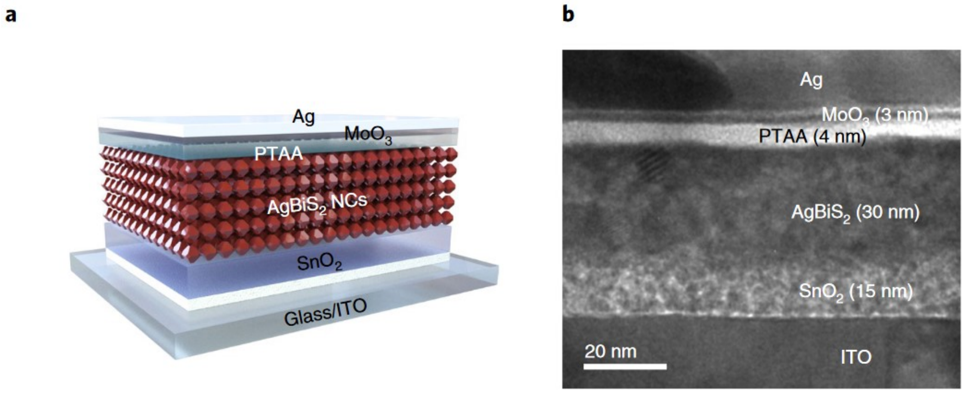

Figure 3.3 Device structure of ultrathin solar cells. *a, Schematic of the AgBiS*$_2$ *(ABS) NC solar cells. b, Cross-sectional TEM image of the device.*

We first used poly[[4,8-bis[(2-ethylhexyl)oxy]benzo[1,2-b:4,5-b’] dithiophene-2,6-diyl][3-fluoro-2-[(2-ethylhexyl) carbonyl] thieno [3,4-b] thiophenediyl]] (PTB7) as an electron-blocking layer, in accordance with previous studies.[58,59] The devices showed an average power conversion efficiency (PCE) of 6.4 ± 0.6%, with a champion device reaching a PCE of 7.6% (Table 3.1)—higher than the previously reported record performance of 6.3% (refs. [58–62,87,88]). Atomic force microscopy (AFM) revealed a surface roughness of 0.6 nm for a 4 nm PTB7 film (Fig. 3.4a), which undermines the performance of the cells by introducing interface recombination.[89]

We sought to replace PTB7 with an alternative electron-blocking layer with improved morphological characteristics. We found that poly (triaryl amine)

(PTAA) yielded improved uniformity (root-mean-square roughness of 0.4 nm), a prerequisite for suppressing current leakage and interface recombination.

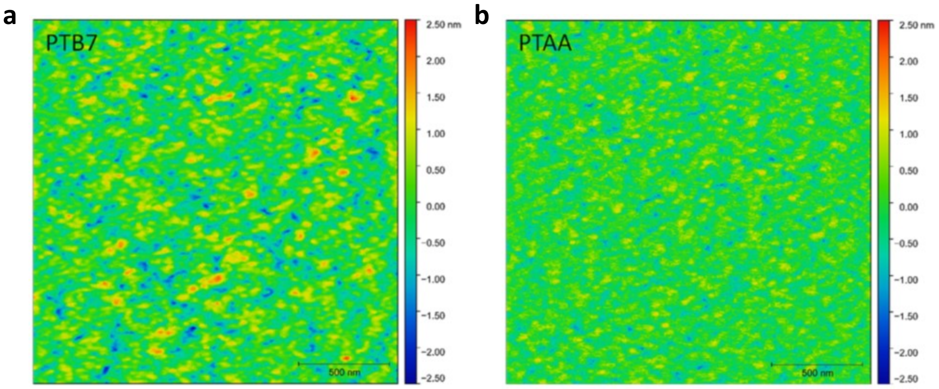

Figure 3.4 Surface morphology of different HTLs. *Atomic force microscope (AFM) images of (a) PTB7 and (b) PTAA on* $AgBiS_2$ *NC films. The RMS roughness for PTB7 and PTAA are 0.6 nm and 0.4 nm, respectively.*

To further assess the superiority of PTAA, transient photocurrent and transient photovoltage were measured under a bias of one sun light (Fig. 3.5). Devices with PTAA showed a faster photocurrent decay and longer carrier lifetime than that with PTB7 as the HTL, which indicates improved charge extraction and reduced interface recombination. As a result, replacing PTB7 with PTAA leads to substantial improvement in V_{oc} and fill factor (*FF*) (Fig. 3.6) and results in an ~20% increase in PCE to 8.7 ± 0.3%, with the best device reaching

9.17% (Fig. 3.7a). One of our champion devices was sent to an accredited photovoltaic calibration laboratory (Newport, USA), which certified the PCE of 8.85% under AM1.5G full-sun illumination, with negligible hysteresis (Fig. 3.7b).

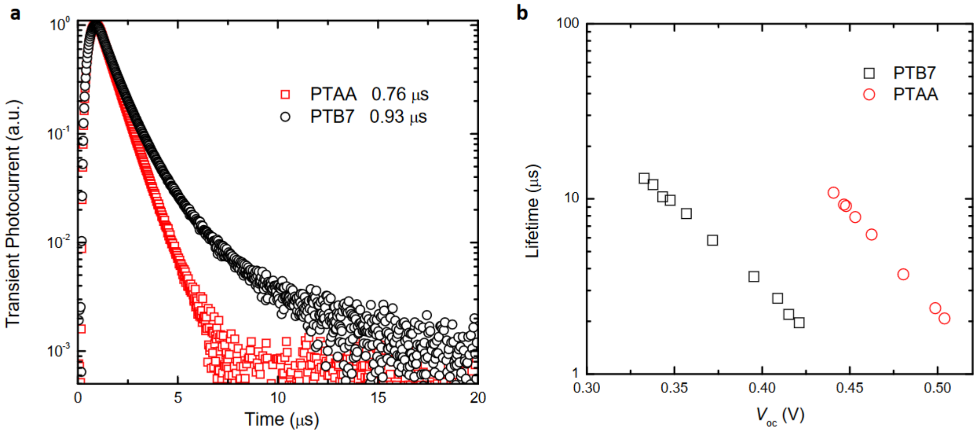

Figure 3.5 Transient photocurrent and photovoltage measurements of devices with different HTLs. *a, Transient photocurrent of devices with PTB7 and PTAA as the HTL. The photocurrent decay lifetime is 0.93 μs and 0.76 μs for PTB7 and PTAA devices, respectively. b, Carrier lifetime extracted from transient photovoltage at different open circuit voltages. Devices with PTAA showed clearly longer lifetime than PTB7 under the same* V_{oc}.

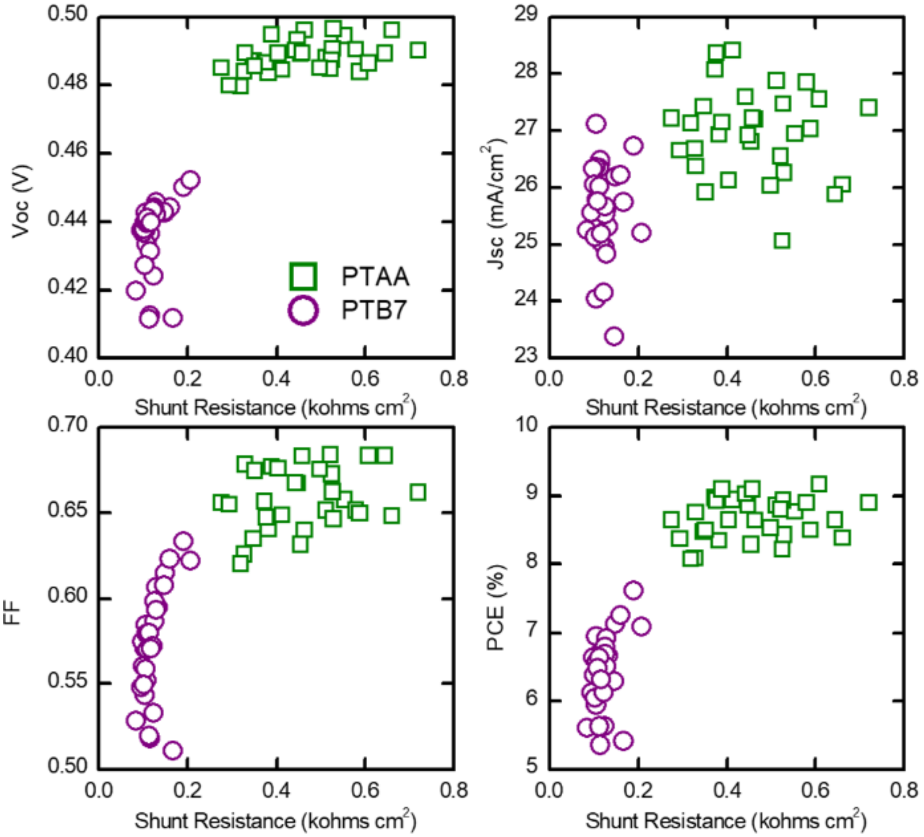

Figure 3.6 Strong correlation of device performance with shunt resistance.

With improved morphology, the PTAA-based devices showed higher shunt resistance and, thus, higher V_{oc} *and FF.*

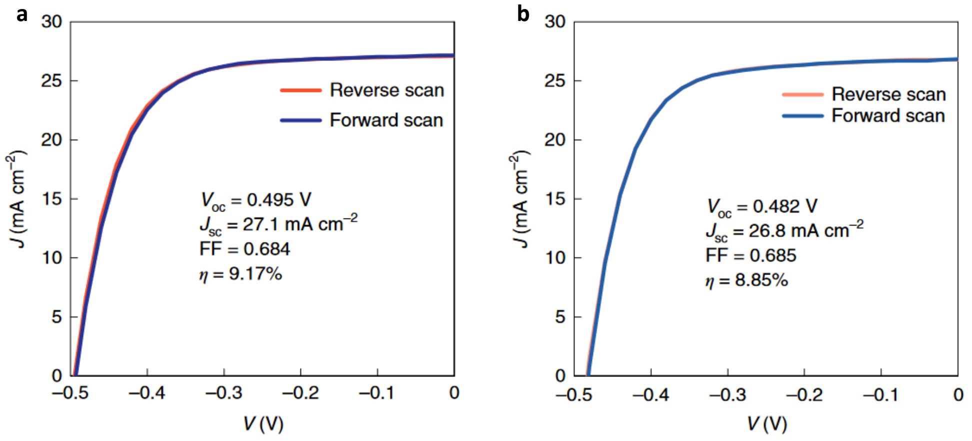

Figure 3.7 Device performance of champion cell. *a, J–V curves of the champion device with PTAA as the HTL. b, J–V curves of AgBiS$_2$ NC solar cells certified at Newport, USA.*

Table 3.1 Photovoltaic parameters of devices based on different HTLs

	V_{oc} (V)	J_{sc} (mA cm^{-2})	Fill factor	PCE (%)
AgBiS$_2$/PTB7	0.437 ± 0.011	25.59 ± 0.81	0.57 ± 0.03	6.42 ± 0.55
Champion device	0.450	26.75	0.63	7.63
AgBiS$_2$/PTAA	0.489 ± 0.005	26.99 ± 0.76	0.66 ± 0.02	8.70 ± 0.31
Champion device	0.495	27.11	0.68	9.17
Certified	0.482	26.8	0.68	8.85

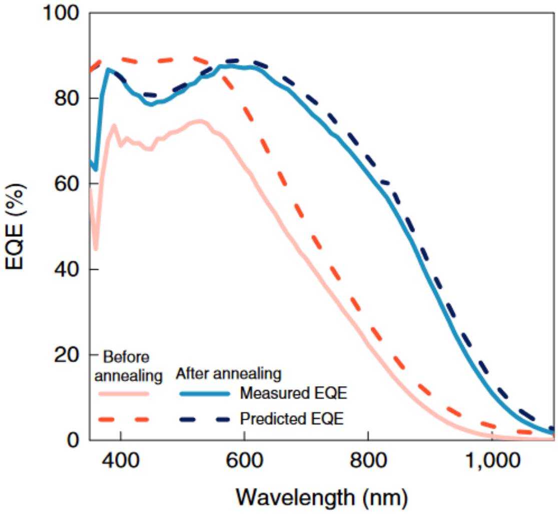

Figure 3.8 Measured and predicted EQE curves of devices before and after annealing.

The measured J_{sc} of 27 mA cm^{-2} was further confirmed by the external quantum efficiency (EQE) spectrum, which gives a value of 26.5 mA cm^{-2} (Fig. 3.8). In addition, the measured EQE spectrum matched well with the TMM-predicted EQE, indicating a near-unity IQE. However, unannealed devices showed not only lower absorption (that is, the predicted EQE) in the near-infrared region but also a lower IQE.

Analyzing the absorption loss of our record-performance ultrathin devices, a large part of the incident light (~10 mA cm^{-2}) was reflected (Fig. 3.9) and further improvement in device performance is expected by introducing an antireflection layer or advanced light-trapping techniques.

In addition to PCE, stability is another important figure of merit of photovoltaic devices. Therefore, to assess the stability of our $AgBiS_2$ NC solar cells, we first measured their shelf lifetime by storing the un-encapsulated devices in ambient conditions (temperature, ~25 °C; relative humidity, ~30%). The device showed a gradual improvement in the first 20 days (Fig. 3.10), which is probably a result of the oxidation of the MoO_x layer and better band alignment. Furthermore, the device retained its original performance after aging for four months.

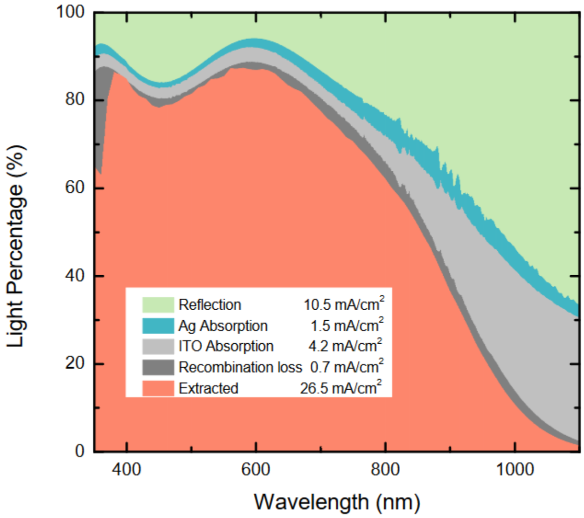

Figure 3.9 Absorption loss analysis of 30 nm thick $AgBiS_2$ solar cell. *A large part of the incident light is reflected (10.5 mA/cm^2) and absorbed by ITO (4.2*

mA/cm^2). The extracted EQE represents the experimentally measured EQE and other EQE curves are obtained from optical simulations.

The operational stability was further investigated by subjecting the un-encapsulated device to AM1.5G one-sun illumination in the ambient atmosphere (relative humidity, ~60%). The device performance was measured by applying a forward bias fixed at the maximum power point (MPP). As shown in Fig. 3.11a, the PCE of the PTB7 device dropped below 2% after 20 min illumination, whereas the PTAA device demonstrated much better operational stability under continuous operation. After 10 h of MPP testing on the un-encapsulated cell in ambient conditions, the device retained 85% of its original efficiency. Longer stability at the MPP was also recorded with a class AA solar light source, showing ~80% of the original performance after 40 h test in ambient air (Fig. 3.11b).

To the best of our knowledge, the devices reported here set a record among low-temperature and solution-processed, non-toxic inorganic solar cells in terms of stability and performance. These results support the fact that $AgBiS_2$ NCs are an extremely promising material for low-cost, efficient, stable and environmentally friendly solar cells.[90–93]

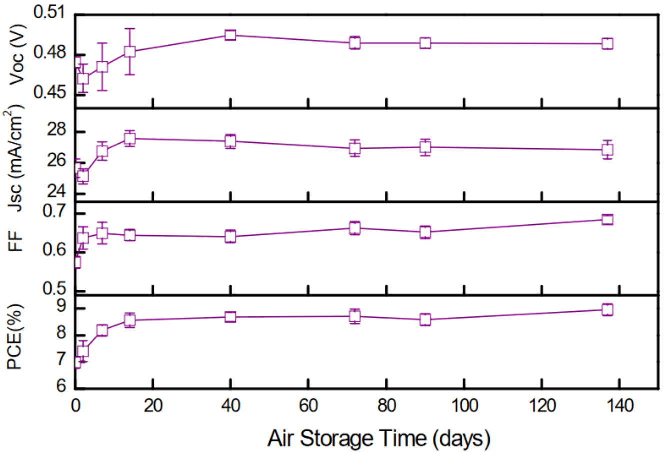

Figure 3.10 Shelf lifetime of AgBiS$_2$ NC solar cells. *The devices were stored in ambient conditions without encapsulation. Data are presented as mean values ± standard deviations.*

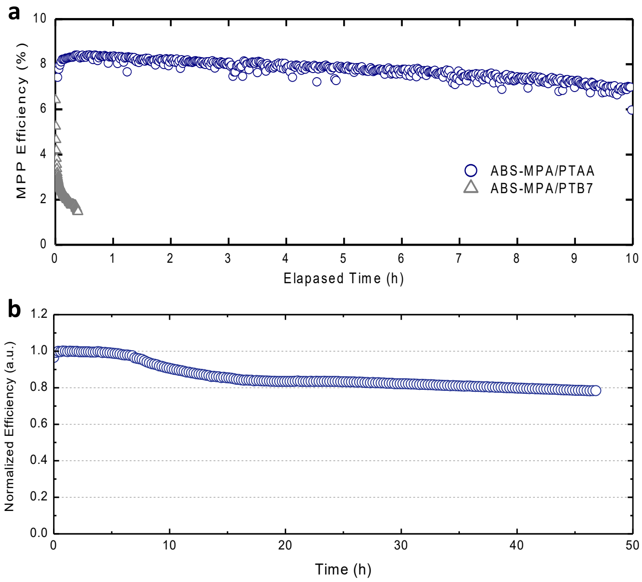

Figure 3.11 Operational stability of 30 nm AgBiS$_2$ NC solar cell under one-sun illumination. *a, MPP test of AgBiS$_2$ devices with PTB7 and PTAA as the*

HTL under AM1.5G AAA solar light. b, Operational stability of PTAA device under a low-cost solar simulator with light from 400 nm to 1400 nm.

The effects of annealing on device performance

In addition to enhanced optical absorption, we also found the annealing process has effects on the electronic properties of NC films. As mentioned before, unannealed devices showed not only lower absorption but also a lower IQE (Fig. 3.8) and larger V_{oc} deficit (Fig. 3.12b). Mid-gap trap density was further estimated from the transient photocurrent/transient photovoltage measurements (Fig. 3.12c&d). The trap density in unannealed devices is ~4 × 10^{17} cm^{-3}, while in our optimal $AgBiS_2$ NC films, the trap density is four times lower, ~9 × 10^{16} cm^{-3}. Hence the lower device performance of unannealed devices can be ascribed to lower absorption together with slower charge extraction, Urbach band tailing and higher trap density.

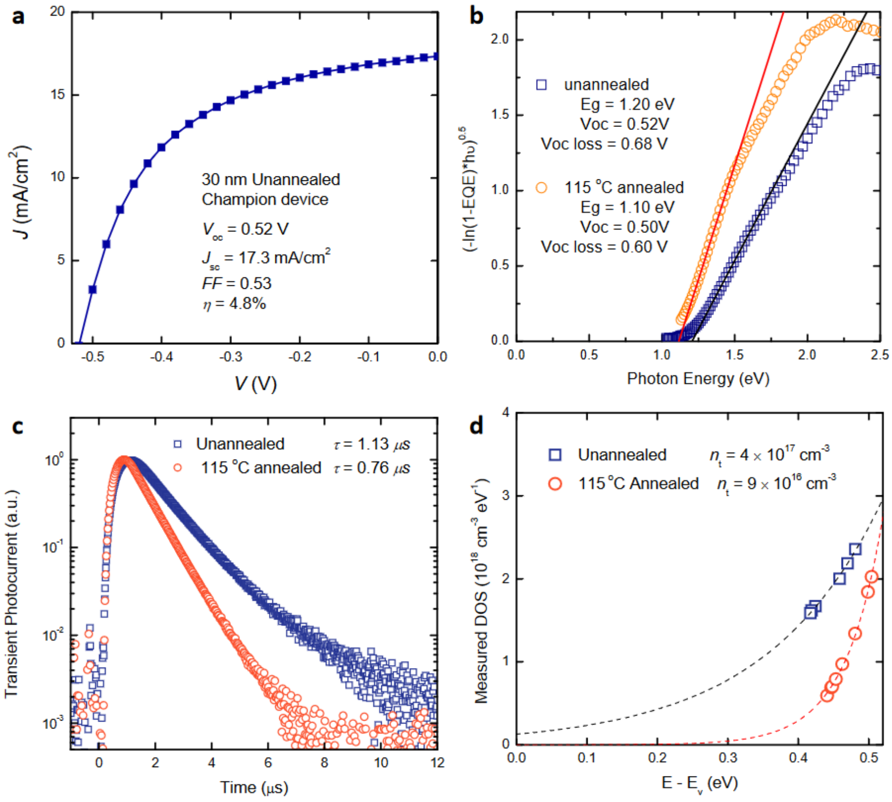

Figure 3.12 Characterization of devices before and after annealing. *a, J-V curve of the champion device without annealing. b, EQE tauc plots of* $AgBiS_2$ *NC devices without and with annealing. c, Transient photocurrent measurement of devices before and after annealing. d, Mid-gap trap density calculated from TPV/TPC measurement.*

Higher-temperature annealing leads to remarkably lower performance, which is consistent with the defects forming from uncontrolled NC fusing (Figs. 2.9 and 3.13).

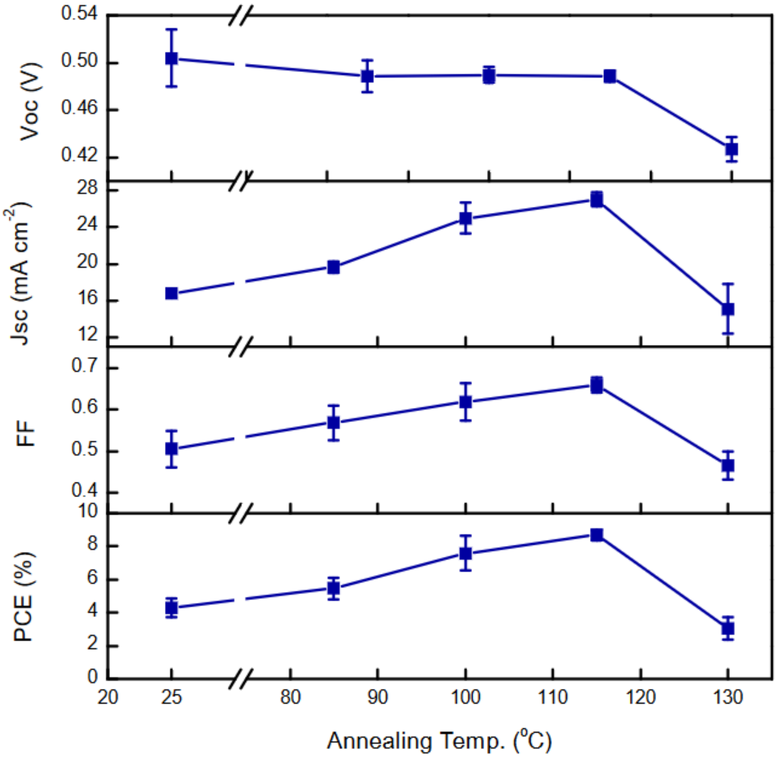

Figure 3.13 Performance of $AgBiS_2$ NCs devices annealed at different temperatures. *Device performance with annealing under different temperatures. The J_{sc} increases with annealing temperature, which is consistent with the absorption coefficient increasing. Devices annealed at 130°C showed lower performance than 115°C, likely due to the uncontrolled nanocrystal fusing and defects forming, as indicated in Fig. 2.9. Data are presented as mean values ± standard deviations.*

On the other hand, thicker (200 nm) devices are also fabricated for direct comparison with ultrathin devices: as expected, a low J_{sc} (~15 mA cm^{-2}) was obtained (Fig. 3.14). To further understand the devices, time-of-flight data were employed to investigate the charge carrier mobilities in our $AgBiS_2$ NC films (Fig. 3.15). The hole and electron mobilities are calculated to be 1.2×10^{-4} and 5.7×10^{-5} $cm^2\ V^{-1}\ s^{-1}$, respectively. Combining with the carrier lifetime extracted from transient photovoltage measurements, the diffusion length is estimated to be ~25.4 nm, which rationalizes the near-unity IQE in our 30 nm devices and the low performance in 200-nm-thick devices.

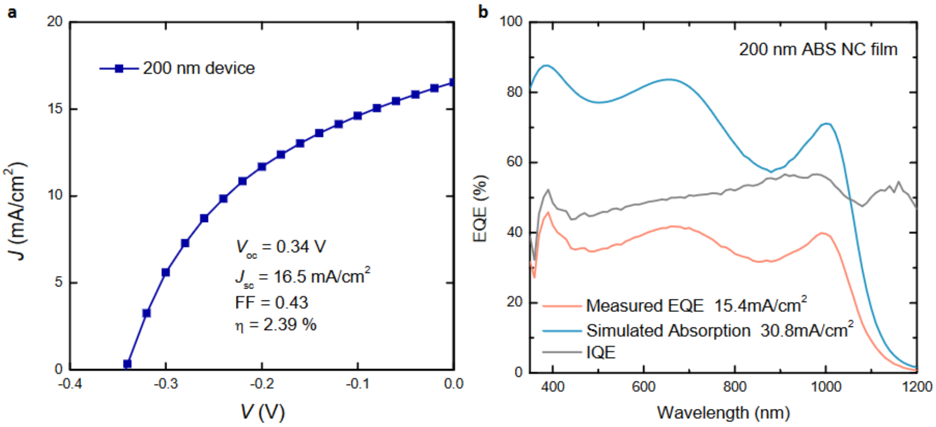

Figure 3.14 Device performance of 200nm thick devices. *a, J-V curve of a typical 200 nm thick $AgBiS_2$ device. b, EQE of a 200 nm thick $AgBiS_2$ device. The low performance and IQE is likely due to a limited diffusion length.*

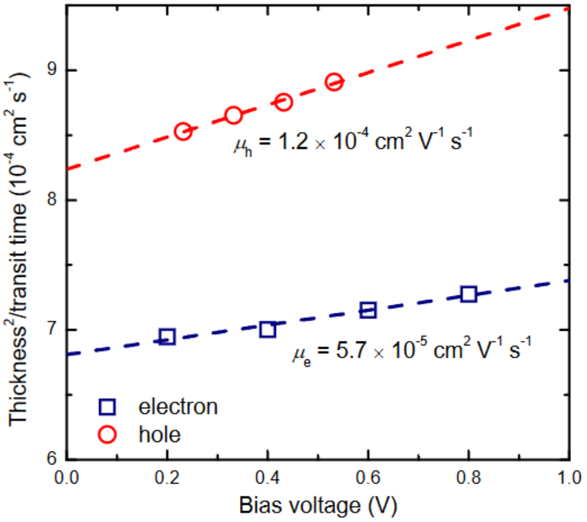

Figure 3.15 Electron and Hole Mobility measurements of 115°C annealed $AgBiS_2$ NC films by Time-of-flight (ToF) method.

Cost analysis of ultrathin solar cells

Apart from the performance improvement in ultrathin solar cells, with the thickness reduction of the $AgBiS_2$ absorber from 500 nm (common photovoltaic thickness) to 30 nm, we expect a huge reduction over the full photovoltaic device cost. For the cost estimation of our ultrathin solar cells, we first estimated the synthesis cost of our $AgBiS_2$ NCs. Based on the chemicals used in our recipe, the cost of oleic acid capped $AgBiS_2$ NCs is ~ 45.5 \$/g. For compatibility with roll-to-roll manufacturing process, we estimated the ink preparation price the same as previously reported for PbS QD ink (~6$/g). In addition to other costs (labour, yield loss, capital expenditure, operation expenditure), the estimated cost for a full device with 500 nm thickness is ~245.2 \$/m^2, with the $AgBiS_2$ absorber layer contributing 128.8 \$/m^2. With the thickness reduced to 30nm, the overall PV cost was reduced ~ 50% to ~125.2 \$/m^2 (with the absorber layer contributing only 7.7 \$/m^2, ~150 mg/m^2), comparable with the estimated cost for perovskite (~128.4 \$/m^2) and lower than PbS QD solar cells (~178.6 \$/m^2).

Table 3.2 Cost breakdown for lab-scale $AgBiS_2$ NC synthesis and ink preparation.

	Price (Euro)	Amount per batch	Cost (Euro)
Silver acetate	11.8 /g	0.534 g	6.3
Bismuth acetate	6.1 /g	1.544 g	9.4
Hexamethyldisilathiane	18.62 /g	0.714 g	13.3
Oleic acid	0.058 /mL	24 mL	1.4
1-Octadecene	0.05 /mL	20 mL	1
Total			31.4 (36.4 $)
$AgBiS_2$-OA NCs Yield		0.8 g	
Ink preparation			6 $/g
Total for ink			51.5 $/g

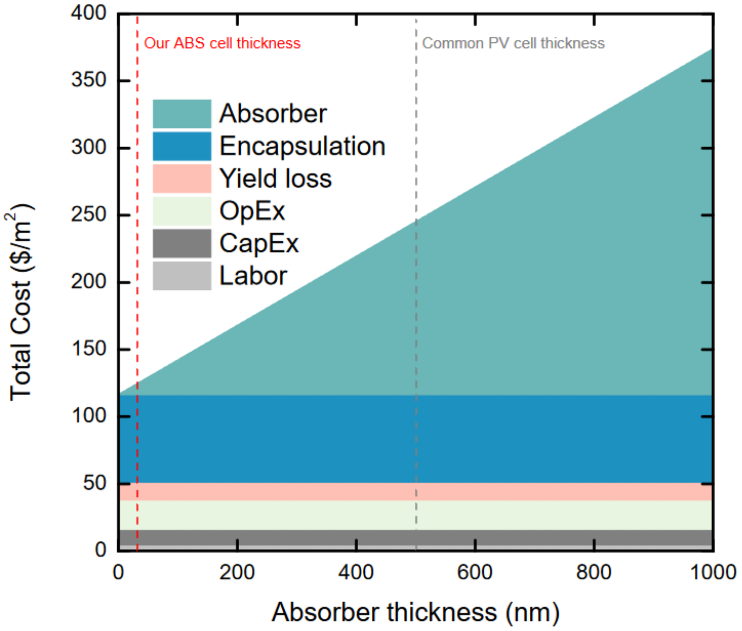

Figure 3.16 Full device cost estimation of $AgBiS_2$ solar cells. *A thickness reduction from common PV thickness of 500 nm to 30 nm will reduce the full device cost ~ 50%. The other costs, except material cost, are taken from reference.*[94]

Table 3.3 Estimated cost of low-temperature solution-processed solar cells.

PV Material		Efficiency (%)	Cost ($/W)
$AgBiS_2$ (30 nm)	Current work	9	1.39
	Projected	15	0.83
	SLME	26	0.48
PbS QDs		14	1.28
Perovskite		26	0.50
Perovskite QDs		18	1.70

Summary

In summary, we have demonstrated that, by optical modelling, high J_{sc} of up to 30 mA cm^{-2} and high efficiency up to 26% can, theoretically, be obtained with only 30 nm $AgBiS_2$ nanocrystal films. Furthermore, ultrathin solar cells are fabricated based on ultra-absorbing $AgBiS_2$ NCs. A high J_{sc} of 27 mA cm^{-2} and a record efficiency of up to 9.17% were obtained with an independent certification of 8.85% from Newport, USA. The air stability and photostability were also recorded in high-performance devices. We further pointed out the beneficial effects of annealing on device performances, in addition to the enhanced absorption. This chapter establishes the potential of ultrathin $AgBiS_2$ NC solar cells, which are solution processable and restriction of hazardous substances (RoHS) compliant.

Chapter 4 Eco-friendly processed aqueous $AgBiS_2$ nanocrystal inks

This chapter is based on the following publication:

Environmentally Friendly $AgBiS_2$ Nanocrystal Inks for Efficient Solar Cells Employing Green Solvent Processing. *Advanced Energy Materials* 2022, 12 (21), 2200700.

Introduction to nanocrystal inks

Colloidal nanocrystals (NCs), promising for various optoelectronic applications, are generally synthesized from wet chemical methods, with long aliphatic molecules serving as surface ligands and giving rise to solution processibility.[28,95] However, for applications that require electronic transport, long insulting organic ligands serve as large barriers, hindering efficient charge transport. In view of this, ligand exchange process has been conducted upon film formation as solid-state ligand-exchange using a layer-by-layer approach. This process being time- and material- consuming is not suitable for large-area high-volume manufacturing required in solar cell industry. To circumvent this, solution-phase ligand-exchange (SPLE) has been recently introduced in NC photovoltaics.[29] Lead chalcogenide nanocrystal inks have been obtained via SPLE methods and high-performance optoelectronic devices have been demonstrated with single-step deposition.[17,29,96]

Solution-phase ligand-exchange process happens between two immiscible solvent phases, for one phase being nonpolar to dissolve organic ligands capped nanocrystals and the other being polar, with high dielectric constants, to provide effective screening of electrostatic attraction between oppositely charged ions.[20] Currently, the most widely used solvents in solution-phase ligand-exchange procedures are formamide (FA), N, N-dimethyl formamide (DMF) and dimethyl sulfoxide (DMSO).[29,61,97,98] However, these polar solvents are highly toxic, raising major concerns on overall environmental impact.[99] Moreover, occupational safety must be taken into account for operators in manufacturing or scientists in the lab, who may come into direct contact with the ink or inhale solvent fumes during fabrication. Investigation of alternatives for ink preparation and device fabrications offers an invaluable opportunity toward safe and up scalable photovoltaic manufacturing techniques.[15,100,101]

Silver bismuth sulfide nanocrystals ($AgBiS_2$ NCs), in view of their favorable bandgap, high absorption and absence of toxic RoHS elements, are promising solution-processable materials for photovoltaic applications.[58,59,61,62,102] Solution-phase ligand-exchange method has been recently introduced into

$AgBiS_2$ NCs, yet their performance has been lower than their solid-state ligand-exchanged counterparts.[61,103] Here, we report a facile solution-phase ligand-exchange method for the production of $AgBiS_2$ inks employing 3-mercaptopropionic acid (MPA) and methanol (MeOH) as the ligand and solvent pair. The resultant MPA capped nanocrystals can be easily dissolved in water, rendering the final ink used for device fabrication, completely environmentally friendly. Furthermore, implementing $AgBiS_2$ nanocrystal inks into fully green-processed photovoltaic devices, an efficiency up to 7.3% was achieved, along with superior air stability.

Solution-phase ligand-exchange of $AgBiS_2$ nanocrystals

The $AgBiS_2$ nanocrystals are first synthesized following a standard air-free Schlenk line technique with oleic acid as the surface ligands.[58,59] Prior to the ligand exchange, nanocrystals were dispersed in octane, and 3-mercaptopropionic acid (3-MPA) was dissolved in methanol as ligand solution, as shown in Fig. 4.1. The nanocrystal/octane was then mixed with MPA/methanol vigorously and the two phases became well-separated immediately. The octane phase was removed carefully, and the methanol phase was washed with octane to remove residual oleic acid ligands. The methanol phase was then centrifuged directly, and the supernatant became colorless after centrifuge, indicating near 100% yield after ligand exchange. The $AgBiS_2$ nanocrystal powder was then dissolved in water/butyl-amine mixture, followed by an additional precipitation with acetone to obtain MPA capped $AgBiS_2$ nanocrystal powder. The nanocrystal powder can be then fully dissolved in distilled water or water/butyl-amine mixture, forming stable aqueous inks with concentration up to 200 mg mL^{-1}.

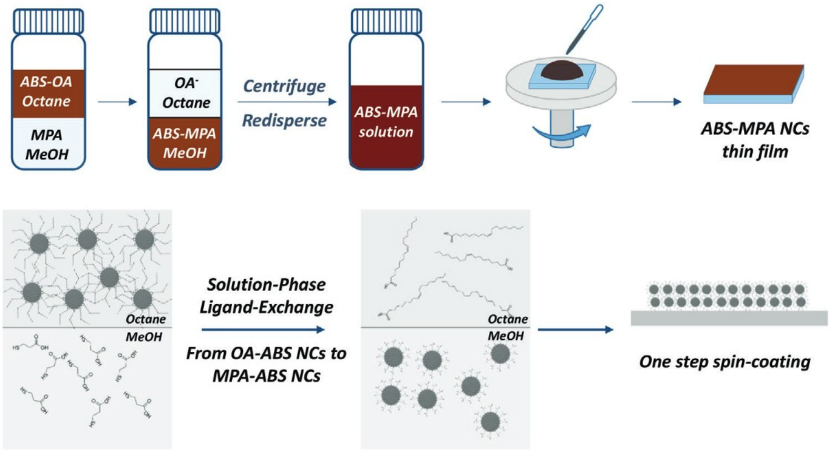

Figure 4.1 Schematics of the solution-phase ligand-exchange process of $AgBiS_2$ nanocrystals.

Fourier transform infrared spectroscopy (FTIR) was used to confirm the successful exchange between oleic acid and MPA ligands. As shown in Fig. 4.2, the characteristic peak of C=C-H bond at ≈ 3005 cm^{-1} from oleic acid disappears after ligand exchange, indicating the near-complete removal of oleic acid ligands.[104,105] Furthermore, no clear peak of S–H at ≈2550 cm^{-1} from the FTIR spectrum indicates the bonding of –SH on the nanocrystal surface. Moreover, the carboxyl group was also partially bound on the nanocrystal surface, as evidenced by the peak around 1550 cm^{-1}.[106] After mixing with butyl-amine, the broad peak centered at around 3000 cm^{-1}, which is from O–H of carboxyl acid group, decreased significantly, indicating the reaction between amine and acid. The amine/acid ion pair forms electrical double layers at the nanocrystal/solvent interface, enabling the dispersion of MPA capped nanocrystals in water.[34,107]

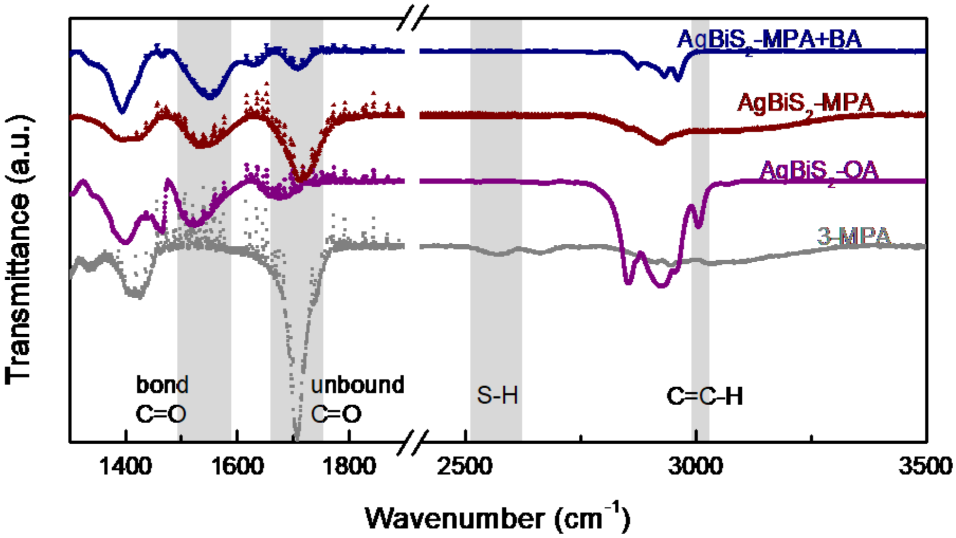

Figure 4.2 Fourier transform infrared (FTIR) spectrum of $AgBiS_2$ *nanocrystals before and after ligand-exchange with MPA.*

Nuclear magnetic resonance spectrum (NMR) was further implemented to characterize the chemical environments in the inks. The alkyl proton peaks of butyl-amine and MPA are shifted significantly from those observed when only butyl-amine, MPA or their mixture in D_2O in the absence of $AgBiS_2$ nanocrystals, which is consistent with the picture of acid/amine ions double layer structure (Fig. 4.3). Furthermore, the larger downfield shift of alkyl protons (#5) also indicates the bonding of thiols on nanocrystals' surface, consistent with the FTIR measurements.[108]

The absorption spectra of $AgBiS_2$ nanocrystals after SPLE revealed that the optical properties of the NCs remained largely intact by the process, showing only a slight redshift, which is commonly observed also in SPLE-based lead chalcogenide nanocrystals (Fig. 4.4a).[29,109] Transmission electron microscopy (TEM) confirms that the nanocrystals remained distinct and well-dispersed in the final aqueous ink with a size of 4.7 ± 1.1 nm (Fig. 4.4a inset). X-ray diffraction (XRD) also shows the expected Schapbachite $AgBiS_2$ crystal peaks in the films deposited from aqueous inks (Fig. 4.4b).

Comparing with previous iodide based solution-phase ligand-exchange method, our procedure only involves organic ligands (MPA) and non-toxic solvents (methanol and octane), making our method not only much cheaper than other halide based methods, but also with superior environmental friendliness. Previous report estimated over 6 \$ g^{-1} cost addition for ink preparation of iodide capped PbS quantum dots.[94] Here, using low-cost ligands and solvents, we estimate a < 1 \$ g^{-1} addition for our $AgBiS_2$ nanocrystal ink. Meanwhile, the final solvent here can be water, leading to a nanocrystal ink fully compatible with established manufacturing industrial processes, such as roll-to-roll and ink-jet printing, for printable devices.

Before building any full device stacks, the surface morphology of the resultant nanocrystal films was investigated. Scanning electron microscopy (SEM) does not exhibit any observable cracks in the single-step deposited films (Fig. 4.5a). Atomic force microscopy (AFM) also confirms the surface roughness of ≈0.8 nm, which indicates the high morphological quality of our single step deposited nanocrystal films (Fig. 4.5b). Furthermore, although butyl-amine was introduced as solvent for our MPA-$AgBiS_2$ nanocrystals, X-ray photoelectron spectrum (XPS) confirms the absence of N 1s peak at 402 eV, indicating the complete removal of butyl-amine after film deposition (Fig. 4.6).

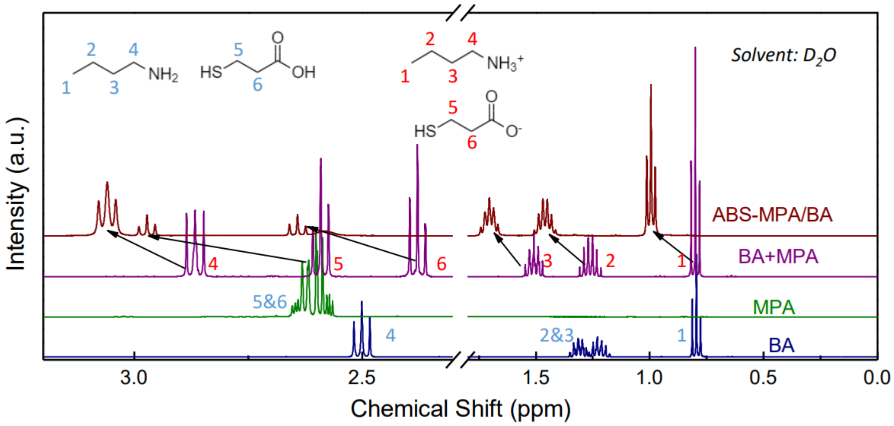

Figure 4.3 Nuclear magnetic resonance spectrum of MPA, butyl-amine (BA), MPA+BA and MPA-AgBiS$_2$ Nanocrystals with BA in D_2O.

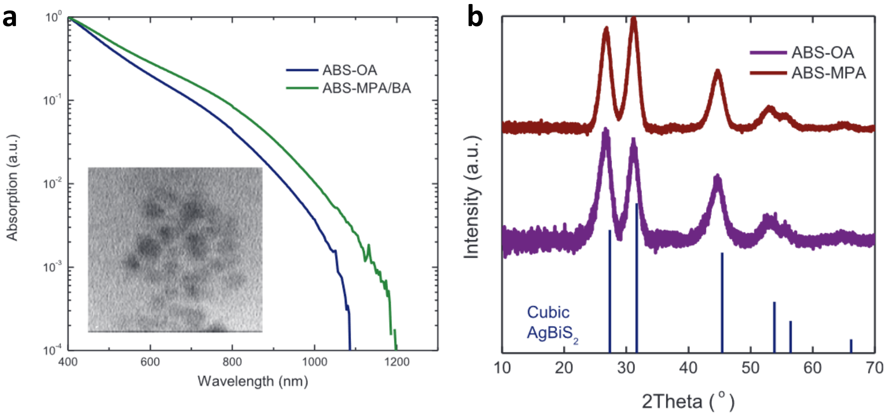

Figure 4.4 Material characterization of AgBiS$_2$ NCs before and after SPLE.

a, Normalized absorption spectrum of AgBiS$_2$ nanocrystals before and after SPLE in solutions. Inset: TEM image of MPA-AgBiS$_2$ nanocrystals from water.

b, X-ray diffraction (XRD) spectrum of AgBiS$_2$ nanocrystal powder before and after SPLE.

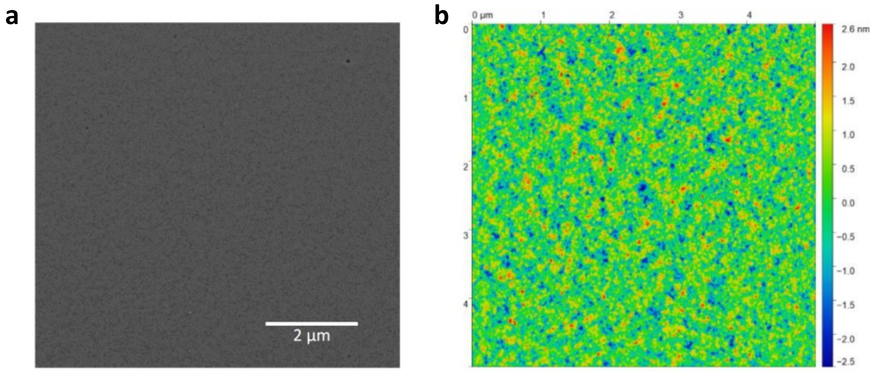

***Figure 4.5 Morphology characterization of AgBiS$_2$ NC films.** a, Scan electron microscopy (SEM) image of MPA-AgBiS$_2$ nanocrystal film. b, Atomic force microscopy (AFM) image of MPA-AgBiS$_2$ nanocrystal films.*

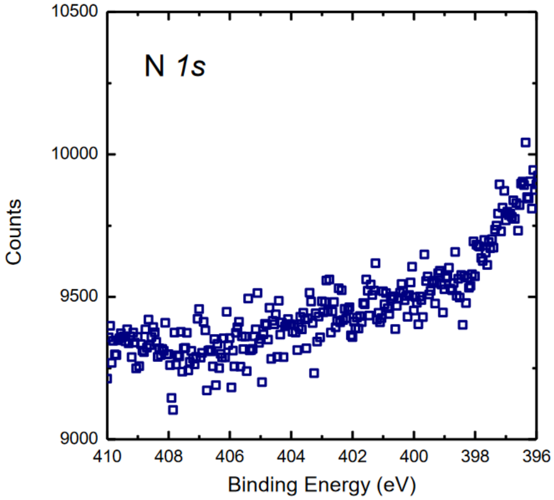

Figure 4.6 N 1s XPS spectrum of MPA-AgBiS$_2$ nanocrystal films.

Solar cell devices based on $AgBiS_2$ nanocrystal inks

Although recent reports of $AgBiS_2$ nanocrystal solar cells indicate the superiority of iodide ligands,[58,60,110] we implemented our MPA-$AgBiS_2$ nanocrystal inks into photovoltaic devices with a configuration same as previous chapter. As shown in Fig. 4.7a, nanocrystal films were deposited onto ITO/SnO_2 substrates with single step spin-coating. On top of nanocrystals, PTAA was deposited as hole transport layer and MoO_3/Ag electrodes were further deposited by thermal evaporation.

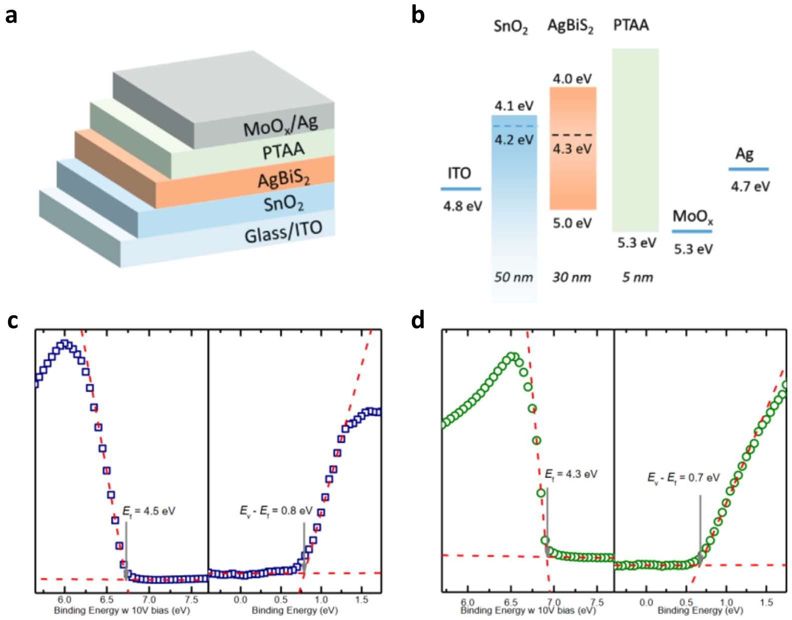

Figure 4.7 Device structure and band alignment. *a, Device configuration and b, band diagram of* $AgBiS_2$ *nanocrystal solar cells. Ultraviolet photoelectron spectrum (UPS) of (c) PTAA and (d) MPA-*$AgBiS_2$ *nanocrystal films.*

The proposed band diagram is shown in Fig. 4.7b. For the electrodes and the charge-extracting layers, we have used values reported in the literature,[111–114] while for the PTAA and $AgBiS_2$ NC layers, the energy level of the conduction and valence band edges have been extracted from ultraviolet photoelectron spectroscopy (UPS) measurements (Fig. 4.7c&d).

Although the valence band offset (VBO) between PTAA and $AgBiS_2$ NCs seems blocking the current, we found it is counterintuitively beneficial according to numerical simulation with SCAPS (Fig. 4.8). This VBO is in analog to the small conduction band offset (CBO) which has been proven favorable for high performance devices in kesterite solar cells.[54,115,116]

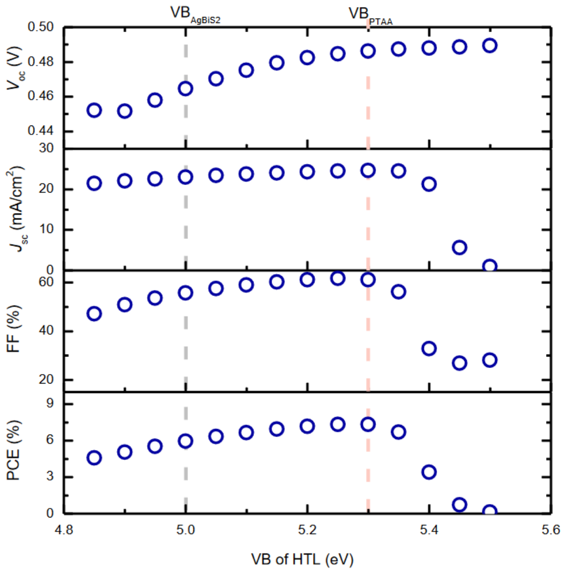

Figure 4.8 Simulated device performance with the valence band (VB) variation of hole transport layer (HTL).

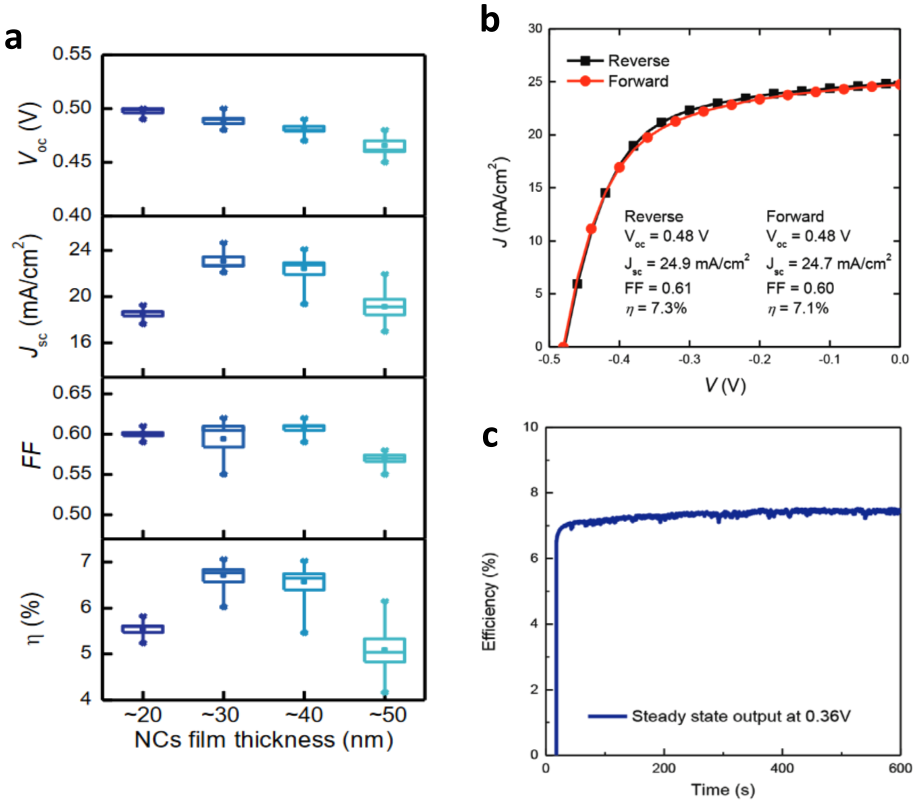

Figure 4.9 Photovoltaic performance of MPA-AgBiS$_2$ NCs devices. *a, Thickness optimization for MPA-AgBiS$_2$ NC devices. b, J–V curves, c, steady-state output @0.36 V of AgBiS$_2$ nanocrystal solar cells.*

The device performance was further measured under AM1.5G illumination. The optimized devices with thickness of ≈30 nm (Fig. 4.9) showed a high power conversion efficiency (PCE) of 7.3%, with an open-circuit voltage (V_{oc}) of 0.48 V, short-circuit current density (J_{sc}) of 24.9 mA cm^{-2} and a fill factor of 0.61, as shown in Fig. 4.9b. This efficiency was further confirmed by steady state maximum power-point output tracking (Fig. 4.9c). The performance reported here is significantly higher than previously reported ink based devices, indicating the superiority of our MPA based solution-phase ligand-exchange method.[61]

The J_{sc} value was also estimated from external quantum efficiency (EQE) spectra (Fig. 4.10), which showed an integrated current density of 24.7 mA cm^{-1}, in good agreement with the J_{sc} from J–V curve measurements.

After storage in ambient air under an average humidity of 30% for one month without encapsulation, the high performance device retained more than 95% of the original efficiency (Fig. 4.11), which confirms the robustness of our nanocrystal inks.

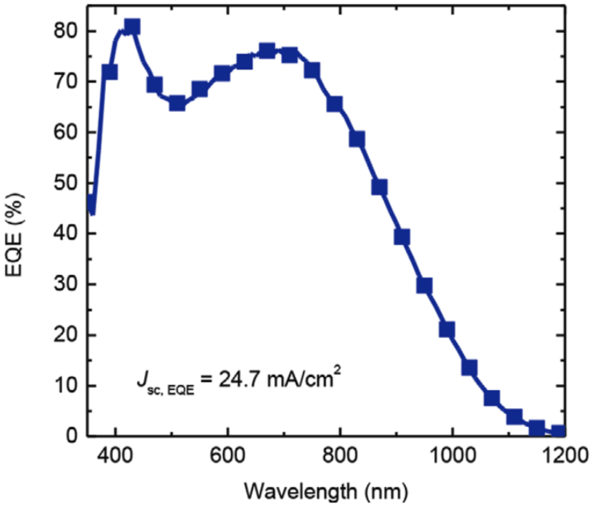

Figure 4.10 EQE spectrum of AgBiS$_2$ nanocrystal devices.

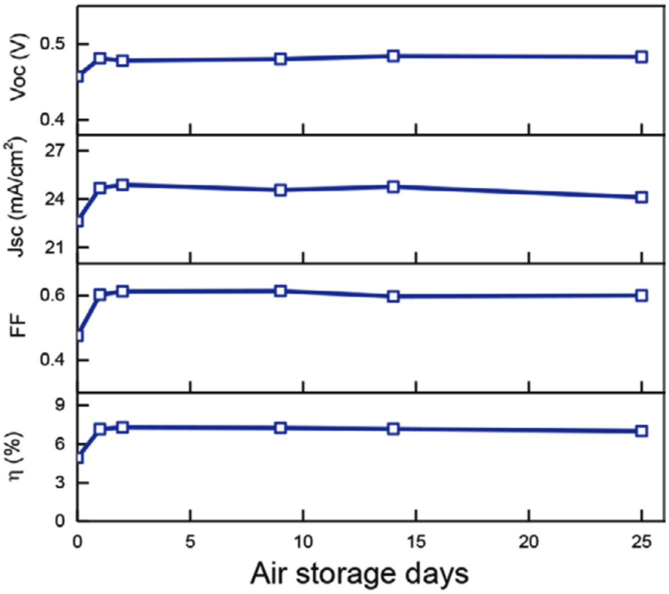

Figure 4.11 Air stability of $AgBiS_2$ nanocrystal solar cells.

Device characterization

To shed more light on the origin of the reported efficiency and understand the limiting factors in our devices, several device characterization techniques were carried out to investigate the working mechanisms. The light intensity dependent J_{sc} and V_{oc} were first measured. The dependence of J_{sc} on light intensity is fitted with a power law expression as $J_{sc} \propto I^{\alpha}$, where I is the light intensity and α is the power factor. As shown in Fig. 4.12a, the extracted α value is 0.92, indicating incomplete charge extraction in the devices. Furthermore, the slope of V_{oc} versus the light intensity gives nkT/e, where n, k, T, and e are the ideality factor, the Boltzmann constant, temperature and the elementary charge, respectively. The diode ideality factor n is an indicator of the dominant recombination mechanism. The fitting of V_{oc} gives an ideality factor of 1.44 (Fig. 4.12b). When band-to-band recombination dominates, n is equal to 1. The ideality factor >1 indicates that other recombination mechanisms such as trap-assisted recombination (n = 2) is present in $AgBiS_2$ nanocrystal devices.

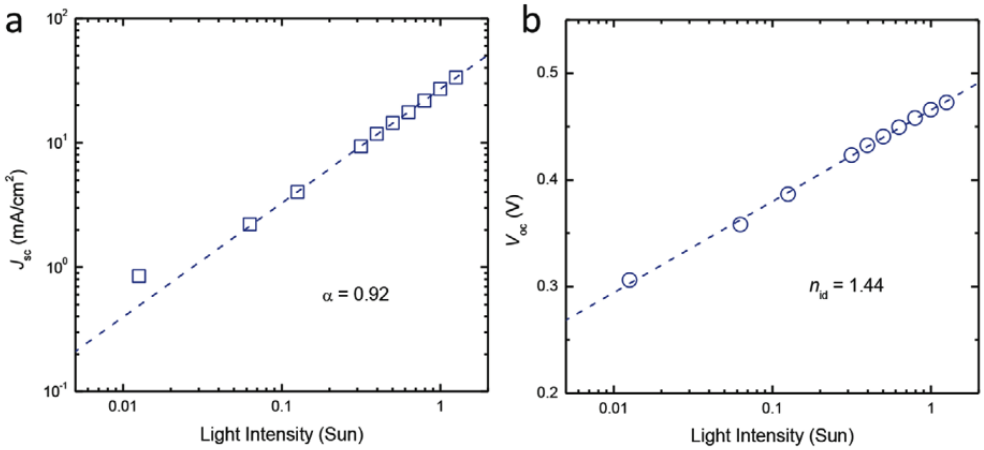

Figure 4.12 Light intensity dependent device performance. *a, Light-intensity dependence of* J_{sc}*. Dash line: linear fit. b, Light intensity dependence of* V_{oc}*. Dash line: logarithmic fit with an ideality factor of 1.44.*

Temperature dependent *J–V* characteristics can provide further insight into the generation–recombination processes contributing to the diode current. *JV* curves are measured under one sun illumination from 150 to 300 K (Fig.

4.13a). The temperature dependent *JV* curves can be fitted with the Shockley diode equation as:

$$J = \frac{R_p}{R_s + R_p}\left\{J_0\left[exp\left(\frac{e(V - JR_s)}{nkT}\right) - 1\right]\right\} + \frac{V}{R_p} + J_{sc}$$

where J and V are the device current and voltage, R_s the series resistance and R_p the shunt resistance, J_0 is the saturation current. The J_0 and J_{sc} are found to decrease with lowering temperature (Fig. 4.13b). For a single thermally activated carrier generation–recombination mechanism, J_0 can be expressed as:

$$n \times \ln(J_0) = -\frac{E_a}{kT} + n \times \ln(J_{00})$$

where E_a is the activation energy and J_{00} is the reverse current prefactor. An activation energy equal to the absorber bandgap implies the dominance of bulk generation-recombination in the absorber. An activation energy smaller than the bandgap often implies the significance of interfacial recombination.[117] Together with ideality factors extracted from temperature dependent *JV* curves (Fig. 4.13c), as shown in Fig. 4.13d, E_a is determined to be ≈1.01 eV, which is very close to the band gap extracted from absorption spectrum (1.11 eV) and EQE plot (1.05 eV) (Fig. 4.14). This result indicates that the device performance is not limited by interfacial recombination, but by trap-assisted recombination in the absorber layer.

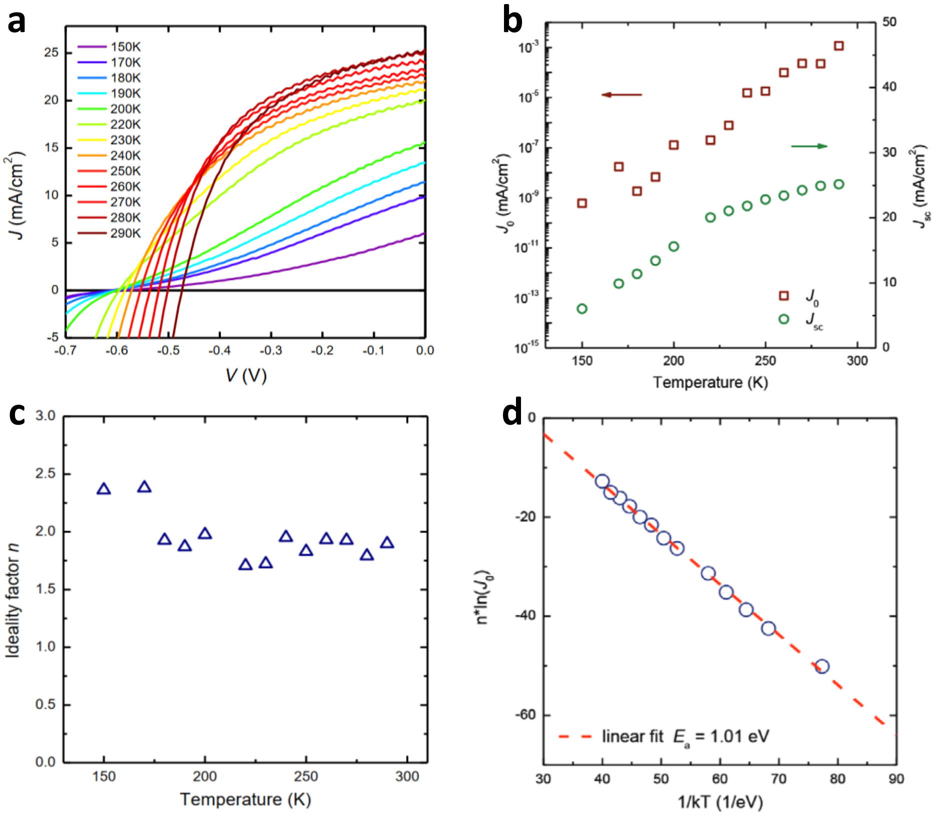

Figure 4.13 Temperature dependent device performance. *a, Temperature dependent JV curves under one sun illumination. b, Temperature dependence of* J_0 *and* J_{sc}*. c, Temperature dependent ideality factors extracted from JV curves. D, Relationship between* $n*\ln(J_0)$ *and 1/kT for estimation of the activation energy* E_a*.*

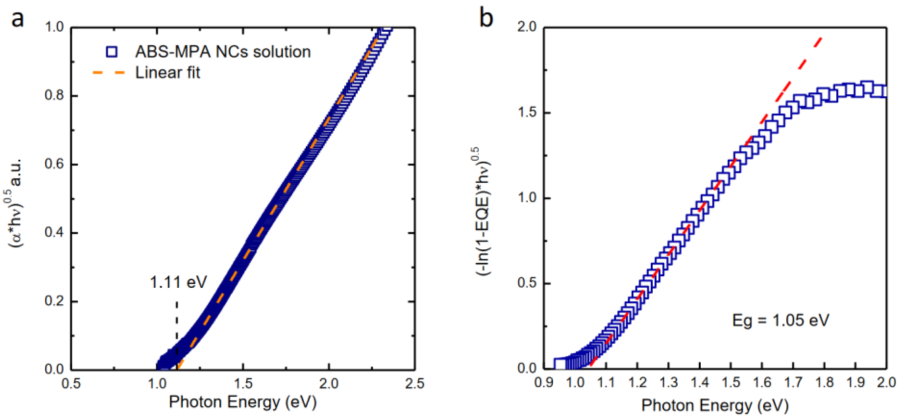

Figure 4.14 Bandgap of AgBiS$_2$ nanocrystals. *Tauc plots of AgBiS$_2$ nanocrystal from (a) solution absorption spectrum and (b) device EQE spectrum.*

In order to evaluate the trap states quantitatively, transient photovoltage (TPV) and photocurrent (TPC) measurements are conducted under different light bias. The transient photovoltages showed a faster decay with increasing light intensity (Fig. 4.15). The extracted carrier lifetime at 1 sun is ≈2.2 μs, similar as previously reported values under 1-sun illumination.[58,59] However, we found longer carrier lifetimes in ink based devices under the same V_{oc}, even comparable with double-injection synthesized larger nanocrystals (Fig. 4.15c). In equilibrium state, carrier recombination cancels the generation and V_{oc} is determined by the number of remaining photo-generated carriers. Longer carrier lifetime indicates slower recombination rate and implies lower trap density in $AgBiS_2$-MPA ink films. The recombination rate in our ink-based devices are further calculated to be on the similar level as other types of nanocrystal devices under one-Sun illumination but higher recombination rate under same V_{oc},[118,119] indicating the necesarity of better surface passivation strategies (Fig. 4.15d).

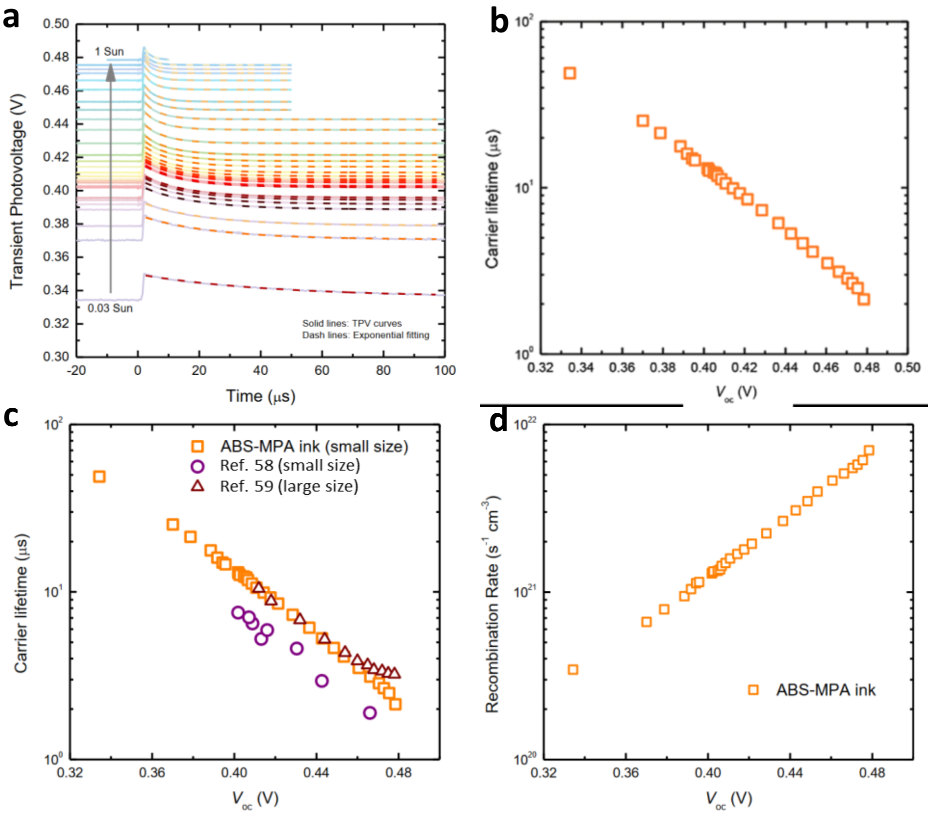

Figure 4.15 Transient photovoltage measurements. *a, Transient photovoltage decays of $AgBiS_2$ NC devices. b, Carrier lifetime as a function of V_{oc}. Lifetimes are determined from the transient photovoltage decays. c, Comparison of the carrier lifetime of ink device and previously reported solid*

state ligand exchanged device. d, Recombination rate of ink-based devices calculated from TPV/TPC data.

Furthermore, in combination with transient photocurrent, mid-gap trap state density is estimated to be ~10^{17} cm^{-3} (Fig. 4.16), which is lower than previously reported halide passivated $AgBiS_2$ nanocrystal films.[61]

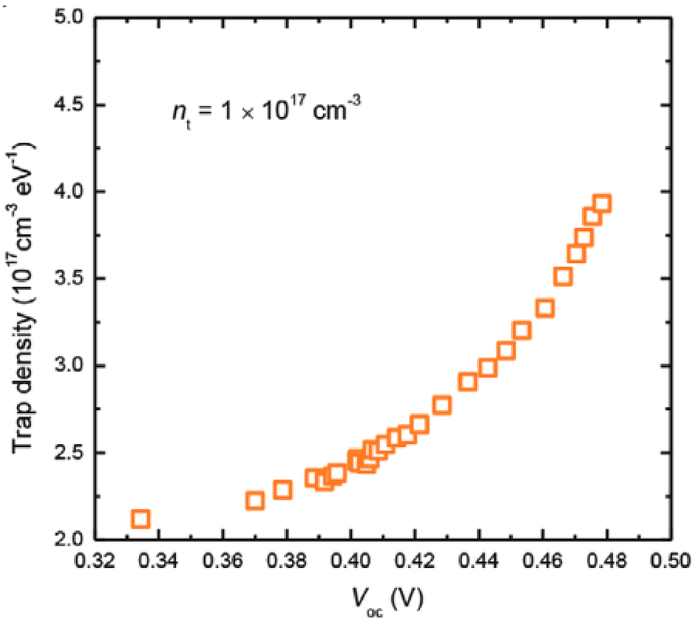

Figure 4.16 Density of trap states in the bandgap calculated from TPV/TPC measurements.

Photo-induced charge carrier extraction by linearly increasing voltage (Photo-CELIV) was further employed for the charge carrier mobility (Fig. 4.17). The measurement yields a mobility of ~ 4.1 ×10^{-5} cm^2/V·s. Together with the lifetime extracted from TPV measurements, the carrier diffusion length was estimated to be ~15 nm. In order to obtain higher power conversion efficiency, further efforts should be put towards trap passivation by advanced surface ligand strategies for higher mobility and longer diffusion lengths.

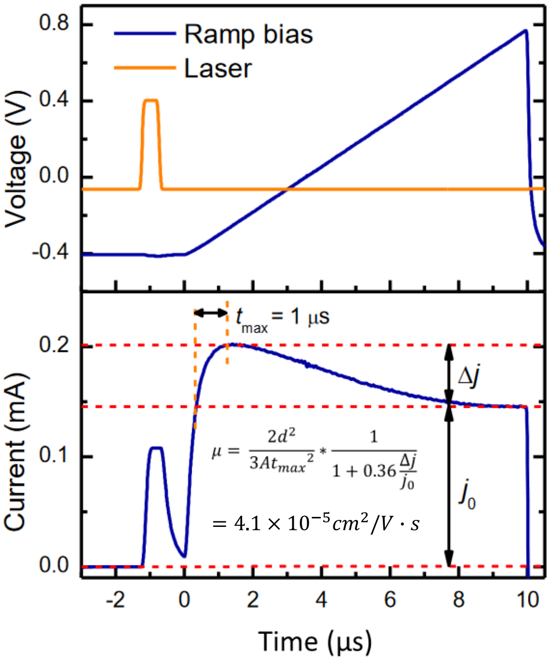

Figure 4.17 Photo-CELIV measurement for carrier mobility.

Summary

In summary, we have developed a method for completely environmentally friendly $AgBiS_2$ nanocrystal inks via solution-phase ligand-exchange. 3-mercaptopropionic acid and methanol are chosen as ligand and solvent pair for fast ligand-exchange with oleic acid capped nanocrystals. Benefiting from the water based $AgBiS_2$ nanocrystal ink, fully green-processed photovoltaic devices are fabricated. A power conversion efficiency up to 7.3% was achieved with superior air stability. Device characterizations were conducted and we pointed out that current devices are limited by trap-assisted recombination in absorber layer. Advanced surface passivation strategies, such as inorganic-organic hybrid surface ligands, may lead to further device performance improvements.

Chapter 5 Conclusions and Outlook

Conclusions

Emerging photovoltaic techniques have progressed rapidly in the last decade. Silver bismuth sulfide ($AgBiS_2$) nanocrystals, possessing superior optical properties, solution-processability, earth-abundance and non-toxicity, are excellent materials for advanced solar cell applications. However, the power conversion efficiency of $AgBiS_2$ nanocrystal based solar cells has been stagnating at ~6% for over five years, leaving them less competitive to other photovoltaic materials.

The device performance is mainly limited by the trade-off between efficient charge extraction and efficient light absorption. The $AgBiS_2$ NC absorber layer needs to be as thick as possible to obtain efficient optical absorption, while the charge extraction requires it to be as thin as possible to yield charges efficiently. This conflict has been leading researchers to extend the device charge extractability, as the optical absorption of a semiconductor has been considered as an intrinsic property, which is impossible to tune. Efforts have been also paid on optical trappings to compensate light absorption, while complicate optical structures often deteriorate the device electronic properties, leading these approaches less effective.

This thesis therefore starts from the fundamental relation between intrinsic optical absorption and atomic arrangements in semiconductor crystals. We showcase the power of cation-disorder homogeneity engineering in the form of optical absorption enhancement – the engineered $AgBiS_2$ nanocrystals showing absorption coefficients higher than any other commonly used solar materials and thus leading to a new record performance.

Summary of findings

In this work, I focused on the material and processing engineering for $AgBiS_2$ nanocrystal solar cells and presented a facile yet advanced tool for solution-processed optoelectronics.

I took the view of fundamental relationship between atomic arrangements and optical properties in multinary semiconductors and further presented a facile annealing procedure that was able to facilitate cation-disorder homogenization in ternary $AgBiS_2$ nanocrystals. The absorption coefficients of $AgBiS_2$ NC films were enhanced by a factor of two, resulting an absorption coefficient higher than any other commonly used solar materials.

I further implemented the ultra-absorbing $AgBiS_2$ NC films into ultrathin solar cells. With the engineering of the hole transporting layer, the devices showed power conversion efficiencies of up to 9.17%, with independent certification of 8.85%, >40% higher than previous world record. The devices also showed excellent shelf stability in ambient atmosphere and promising operational stability. This works demonstrated the power of cation-disorder homogenization and the benefits of HTL engineering in the form of photovoltaic device performances.

In addition, I developed a solution-phase ligand-exchange process for aqueous nanocrystal inks, which can be deposited as the absorber layer, without requiring chemical post-treatments. I further showed that the single-step deposited films have homogenous, crack-free morphologies. This strategy further contributed to solar cells with power conversion efficiency of 7.3%, much higher than previous art of ink devices. This work offered a new platform for eco-friendly nanomaterials with advanced printability and potentially filled the gap between lab-scale device fabrication and massive manufacturing processes.

In summary, this thesis leveraged the relation between atomic arrangements and optical absorption in ternary semiconductors and developed a solar material with the highest absorption coefficients over a wide range of 400 to 1000 nm. Furthermore, through device architecture and ligand-exchange engineering, not only power conversion efficiency, but also the device stability and processibility of $AgBiS_2$ nanocrystal solar cells were substantially improved (Fig. 5.1). This thesis demonstrated the importance of atomic configuration engineering in multinary systems and established the potential of ultrathin $AgBiS_2$ NC solar cells, which are solution processable and restriction of hazardous substances (RoHS) compliant.

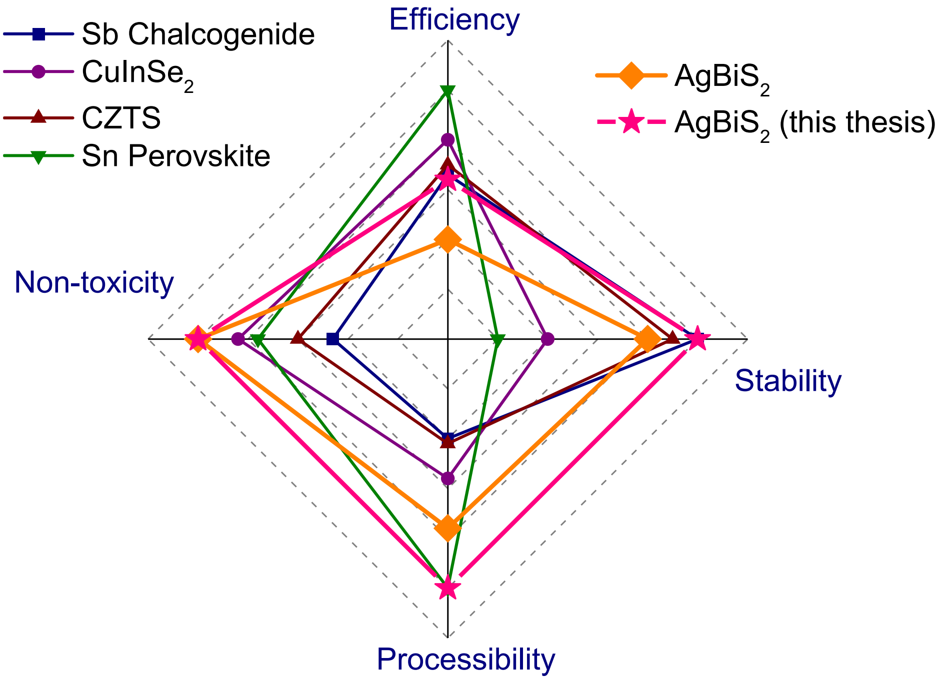

Figure 5.1 Comparison of most important properties of environmentally friendly solar materials after this thesis.

Future work

One of the main topic in this thesis is the cation-disorder homogenization. It is believed that the cation-disorder segregation in ternary $AgBiS_2$ nanocrystals was introduced during the synthesis stage and is due to the reactivity difference between two cation precursors. Thus, tuning the reactivity of precursors and synthesizing homogenous cation-disordered $AgBiS_2$ nanocrystals is a promising strategy to further improve the device performance.

Control over the doping properties also helps forwarding the progress of $AgBiS_2$ nanocrystal solar cells. Homo-junction between different doped $AgBiS_2$ nanocrystals would enable a wider built-in electric field and charge separation/extraction without sacrificing light absorption. Furthermore, with the configuration of gradient doped $AgBiS_2$ nanocrystals, the electric field can be extended to cover the whole device, maximizing the charge drift and collection efficiency.

The device performance is currently limited by the open-circuit voltage. Open-circuit voltage can be interpreted as quasi-fermi-level split in absorber layer under light illumination. As demonstrated in Chapter 4, the open-circuit voltage is mainly limited by the trap states in the absorber layer. Investigations towards the origin of trap states are urged and strategies to eliminate them are further necessitated for device performance improvement. Improving open-circuit voltage in $AgBiS_2$ nanocrystal solar cells could potentially lead to huge leaps in power conversion efficiencies.

Nanocrystal superlattice could be another powerful platform for efficient optoelectronic devices. Long range ordered nanocrystal superlattice can show band-like transport with very high mobility, a cornerstone for high performance devices. However, due to the size non-uniformity and deficient control of assembly, achieving a large area (> $1cm^2$) device-level superlattice that is suitable for solar cells is unquestionably a formidable task.

Appendices

A Experimental Section of Chapter 2

Synthesis of $AgBiS_2$ *NCs.* The Schlenk technique was used to synthesize $AgBiS_2$ NCs, following a previous report with modifications.[58,59] Briefly, 4 mmol $Bi(OAc)_3$, 3.2 mmol Ag(OAc), 24 ml oleic acid and 15 ml 1-octadecene were pumped at 100 °C for 2 h (~0.2 mbar) to remove oxygen and moisture. All solids should be dissolved at this stage and the precursor should be clear and colorless. Then, 4 mmol hexamethyldisilathiane dissolved in 5 ml 1-octadecene was quickly injected into the flask under argon atmosphere at 100 ºC. The heating mantel was removed after injection and the reaction was cooled down in a water bath for ~5 min. After that, the crude solution was stirred for 1 h at room temperature. The NCs were isolated by adding acetone (volume ratio ~1:1), followed by centrifugation at 4500 rpm for 5 min. The extracted NCs were redispersed in 30 mL toluene, and 30 mL acetone was added to precipitate the NCs. The redispersion/precipitation was repeated once more with 20 mL toluene and 20 mL acetone. Finally, the obtained $AgBiS_2$ NC powder was dispersed in anhydrous toluene (20 mg ml^{-1}) and stored in the ambient atmosphere for device fabrication. Generally, the yield per batch is around 750 mg $AgBiS_2$ NCs.

Characterization of $AgBiS_2$ *NCs and films.* Films exchanged with 3-mercaptopropionic acid (MPA) were grown on glass substrates, followed by annealing at different temperatures in a glovebox. The thicknesses were measured using a profilometer. The complex refractive index was measured at various angles using a broadband Sopra Ellipsometer GES5E instrument. The SEMILAB spectroscopic ellipsometry analyser software was utilized to fit a model of stacked layers of appropriate optical constants and the thickness from the profilometer was used as an input. The absorption coefficients are calculated from the extinction coefficients. For XRD samples, $AgBiS_2$ NCs solution was mixed with MPA/methanol solution, leading to a precipitation of ligand-exchanged NCs. The NCs were further centrifuged, washed twice with methanol and once with toluene, mimicking the spin-coating process. The NCs powders were then placed on sample holder for XRD measurement. The XRD data were collected using a Rigaku SmartLab powder diffractometer in the Bragg–Brentano geometry with Cu Kα radiation. XPS samples were prepared by depositing $AgBiS_2$ NCs onto ITO substrates. The XPS measurements were performed with a SPECS PHOIBOS 150 hemispherical analyzer under ultrahigh-vacuum conditions (10^{-10} mbar), with a monochromatic Kα X-ray source (1,486.74 eV) at the Institut Català de Nanociència i Nanotecnologia. TEM samples are prepared by dropping diluted NC solution onto ultrathin carbon TEM grids. The TEM grids were further immersed in MPA/ methanol ligand solution, pure methanol and toluene for ligand-exchange. TEM was performed at the Scientific and Technological Centres of the University of Barcelona. The TEM images were obtained using a JEOL 2100 microscope operating at an accelerating voltage of 200 kV.

B Experimental Section of Chapter 3

Optical modelling and SLME. A home-made MATLAB (R2021a) code was used to implement the transfer matrix formalism. We assumed that each layer was flat and considered no scattering effects. The short-circuit current density was calculated with the assumption of 100% IQE.

The TMM code for normal incidence can be summarized as following:

Main TMM function:

```
load('nk_data.mat');
device_structure = {Glass, ITO1, ITO2, SnO2, ABS, PTAA, MoOx,
Ag, Air};
layer_thickness = { 1,50,50,20,30,3,3,100,100};
num_absorberlayer = 5;
wavelength = Air(:,1);
for i = 1:size(device_structure, 2)
    n(:,i) = device_structure{1,i}(:,4);
    d(1,i) = layer_thickness{1,i}(1,1);
end
Spectrum = zeros(size(n,1), 4);
EQE = zeros(size(n,1),4);
for j = 1:size(n, 1)
   lambda = wavelength(j,1);
   M = zeros(2,2, size(layer_thickness, 2));
    for k = 1:size(layer_thickness, 2)-1
        M(:,:,2*k-1) = I_s(n(j,k), n(j,k+1));
        M(:,:,2*k) = L(n(j, k+1),d(1,k+1),lambda);
    end
    S = Mtrx_Mtp(M, 1, size(M,3)-1);
    r_s = S(2,1)/S(1,1);
    t_s = 1/S(1,1);
    n_glass = device_structure{1,1}(j,4);
    n_air = device_structure{1,size(device_structure,
2)}(j,4);
    R0 = (n_air - n_glass)^2/(n_air + n_glass)^2;
    R_s = (abs(r_s))^2;
    T_s = n_air/n_glass*(abs(t_s))^2;
    Spectrum(j,1) = lambda;
    Spectrum(j,2) = (R_s -2*R_s*R0+R0)/(1-R_s*R0);
    R_total = Spectrum(j,2);
```

```
      Spectrum(j,3) = R0*T_s;
      Spectrum(j,4) = 1 - Spectrum(j,2) - Spectrum(j,3);
      I_in = (1-2*R0+R0*R_total)/(1-R0);
      EQE(j,1) = lambda;
      SumAbs = LayerAbs(M,2*(num_absorberlayer-1),lambda,
n(j,num_absorberlayer), d(1,num_absorberlayer));
      EQE(j,2) = I_in*SumAbs/real(n_glass);
end
```

Interface matrix function:

```
function M = I_s(a,b)
    r = (a-b)/(a+b);
    t = 2*a/(a+b);

    M = (1/t)*[1 r; r 1];
End
```

Propagation matrix function:

```
function M = L(n, d, lambda)
    b = 2*pi*d*n/lambda;
    a = exp(-1*1i*b);
    M = [a 0; 0 1/a];
end
```

Matrix multiplication function:

```
function S = Mtrx_Mtp(M, ls, le)
        S = M(:,:,ls);
        for i = ls+1:le
            S = S*M(:,:,i);
        end
end
```

Absorption in specific layer function:

```
function [SumAbs, Absorption_s] =
LayerAbs(M,layMtrx_num,lambda, n_absorber, d_absorber)
SL = Mtrx_Mtp(M, 1, layMtrx_num -1);
SR = Mtrx_Mtp(M, layMtrx_num +1, size(M,3)-1);
zeta = 2*pi*n_absorber/lambda;
for x = 1: d_absorber
    as = SR(1,1)*exp(-1i*zeta*(d_absorber-x));
    bs = SR(2,1)*exp(1i*zeta*(d_absorber-x));
```

```
     cs = SL(1,1)*SR(1,1)*exp(-1i*zeta*d_absorber);
     ds = SL(1,2)*SR(2,1)*exp(1i*zeta*d_absorber);
     Es = (as+bs)/(cs+ds);
     Is =  abs(Es)^2;
     Absorption_s(1,x)=
4*pi*imag(n_absorber)*Is*real(n_absorber)/(lambda);
end
SumAbs = sum(Absorption_s);
```

Solar cell fabrication. All the solar cell fabrication steps were performed in ambient air, unless with specific descriptions. Unpatterned ITO-covered glass substrates (Universität Stuttgart, Institut für Großflächige Mikroelektronik) were cleaned by ultrasonication in soapy water, acetone and isopropanol for 20 min each and dried with nitrogen, followed with 0.5 h ultraviolet/ozone treatment. SnO_2 electron transport layer was then spin cast from diluted Alfa SnO_2 colloid solution (1:5.6 v/v with H_2O) at a spin speed of 2,000 r.p.m. and annealed at 270 °C for 15 min in ambient atomsphere. The thickness of SnO_2 should vary with the roughness of ITO substrate accordingly. It was observed that devices showed higher reproducibility but less operational stability with thicker SnO_2 layer. Afterwards, three layers of $AgBiS_2$ NCs were deposited from 20 mg ml^{-1} toluene solution via the layer-by-layer method. For each $AgBiS_2$ NC layer, one drop of $AgBiS_2$ NC solution was spin coated onto SnO_2/ITO substrates during spinning (2,000 r.p.m.). Then, 3-MPA/methanol (1% v/v) solution was applied to the NC film for 45 s, followed by two rinse–spin steps with methanol (~40s per step to let NC film completely dry @RH40%, longer time should apply for higher humidity) and once with toluene. The films were transferred into the glovebox for 10 min annealing at 115 °C and then stored in dry air before spin coating PTB7 (5 mg ml^{-1} in dichlorobenzene) or PTAA solution (2 mg ml^{-1} in toluene) at 3,000 r.p.m. Finally, a Kurt J. Lesker NANO 36 system was used to deposit 3 nm MoO_3 and 120 nm Ag through a shadow mask to produce solar cells with a diameter of 2 mm (area, 3.14 mm^2). It was observed that for devices made at high humidity, the dry-air storage time should be extended up to weeks for best performance. A sealed box filled with high-quality desiccant (e.g. silica gel) could be a good substitute to dry-air desiccator. PTAA from different producers were compared and no obvious difference was observed.

Solar cell characterization. All the device characterizations were performed in air under ambient conditions. Current–voltage (J–V) measurements were performed with a Keithley 2400 sourcemeter and a Newport Oriel Sol3A solar simulator with an AM1.5G filter. The intensity of solar light was calibrated using a Hamamatsu S1336 silicon photodiode that was calibrated at the Fraunhofer Institute of Solar Energy Systems. The solar cells were measured with and without masks, and a slightly lower V_{oc} was observed when measuring with masks due to the masking effect. For certified cells, appropriate masks were always used. The EQE was measured using a Newport Cornerstone 260 monochromator, a Thorlabs MC2000 chopper, a Stanford Research SR570 transimpedance amplifier and a Stanford Research SR830 lock-in amplifier. A calibrated Newport 818-UV photodetector was used as the reference. The shelf stability was obtained from the devices stored in air without encapsulation. For the MPP measurement, the MPP voltage (t = 0) was measured before MPP testing. The device was then held at the MPP voltage (t = 0) for the operation stability test. The device was un-encapsulated under AM1.5G illumination. All the devices were characterized under ambient conditions (relative humidity, >60%; ambient temperature, ~25 °C). Longer-time photostability was measured with a low-cost solar simulator from Abet Technologies. Transient photocurrent and transient photovoltage of the devices were measured with a home-made setup. This setup comprises a light-emitting diode lamp (to provide steady-state white-light bias), a 637 nm laser (perturbation) and an Agilent 4000X oscilloscope. The V_{oc} values of the devices are controlled by the light intensity of the light-emitting diode lamp, and the transient voltage induced by the laser pulse are controlled within 5% of the V_{oc} value. The time-of-flight method is used for the mobility measurements. Electron-only and hole-only devices are fabricated with the structure of ITO/SnO_2/$AgBiS_2$/Phenyl-C_{61}-butyric acid methyl ester ($PC_{60}BM$)/Ag and ITO/NiO_x/ $AgBiS_2$/PTAA/MoO_x/Ag. The thickness of the $AgBiS_2$ layer was controlled to ~200 nm. A 520 nm nanosecond laser was used as the excitation light. Photocurrent decay was recorded at various biases with an oscilloscope. The mobility was calculated by fitting the $d^2/t - V_{\text{bias}}$ plots, where d is the thickness, t is time and V_{bias} is the bias voltage.

C Experimental Section of Chapter 4

$AgBiS_2$ Nanocrystal Synthesis. $AgBiS_2$ nanocrystals are synthesized following previous reports.[58,59] Briefly, 8 mmol bismuth acetate $Bi(OAc)_3$, 6.4 mmol silver acetate AgOAc and 136 mmol oleic acid (OA) were pumped overnight at 90 °C to remove oxygen/moisture and form metal oleate precursors. The temperature was then raised up to 100 °C and hold for one more hour. The atmosphere was then switched into argon. 8 mmol hexamethyldisilathiane (HMS) together with 40 mL pre-dried 1-oactadecene (ODE) was injected into the metal oleate precursors swiftly. The reaction solution changed into dark brown color immediately. The heating was stopped and the reaction flask was let cooling down naturally without removing mantel. After cooling of $\approx$2 h, the nanocrystals were precipitated with acetone (v/v 1:1) and centrifuged at 4000 rpm for 5 min. The nanocrystals were further dissolved in toluene and precipitated once more with acetone. The final nanocrystal powder was dissolved in octane to prepare a solution with concentration of 100 mg mL^{-1} for further use.

Solution-Phase Ligand-Exchange for Nanocrystal Inks. 1 mL 100 mg mL^{-1} $AgBiS_2$-OA nanocrystal solution was diluted with 9 mL octane to prepare 10 mL solution with concentration of 10 mg mL^{-1}. 500 μL 3-MPA was dissolved in 10 mL methanol as ligand solution. The $AgBiS_2$/Octane solution was added into MPA/MeOH solution and shaken vigorously to facilitate the ligand-exchange. The two phases became well-separated immediately after stop shaking. The supernatant octane phase was removed carefully and the MeOH phase was washed with 10 mL octane for three more times. 10 mL toluene was then added into MeOH phase and the solution was centrifuged at 3000 rpm for 5 min. The nanocrystal pellet was then fully dissolved in water/ butylamine (4:1 w/w). This solution can be used for device fabrication, while the colloid stability is not satisfying and cannot be kept for further use. Thus, the solution was precipitated with acetone. The final powder was vacuum dried for 20 min and stored in nitrogen filled glovebox for further use. The MPA capped nanocrystal powder can be fully dissolved in water or water/butyl-amine mixture with concentration up to 200 mg mL^{-1}. The nanocrystal/water solution can be stable for one week in dark, while with the addition of butyl-amine, nanocrystals precipitate after one day. *Characterization of AgBiS$_2$ Nanocrystals.* UV–vis absorption measurements were performed with a Cary 5000 spectroscopy in solutions. TEM measurements were performed in the Scientific and Technological Centers of the University of Barcelona (CCiT-UB). TEM micrographs were obtained using a JEOL 2100 microscope. XRD samples were prepared by drop-casting NCs solution onto glass substrates. XRD data were collected using a Rigaku Smartlab powder diffractometer in Bragg-Brentano geometry with Cu Kα radiation. XPS and UPS measurements were performed with a SPECS PHOIBOS 150 hemispherical analyzer (SPECS GmbH, Berlin, Germany) in ultra-high vacuum conditions (10^{-10} mbar), with a monochromatic Kα x-ray source (1486.74 eV) at the Institut Catala de Nanociencia i Nanotecnologia (ICN2).

Device Fabrication and Characterization. ITO covered glass substrates (Universität Stuttgart, Institut für Großflächige Mikroelektronik) were cleaned by ultrasonication in soapy water, acetone and isopropanol for 20 min each and dried with nitrogen, followed with 30 min UV/ Ozone treatment. SnO_2 electron transport layer was then spin cast from diluted Alfa SnO_2 colloid solution (1:1 v/v with H_2O) with spin speed of 2000 rpm and annealed at 270 °C for 15 min. 50 mg $AgBiS_2$-MPA nanocrystal powder was dissolved into 1 mL water/butylamine (4:1 w/w) to prepare an ink with concentration of 50 mg mL^{-1}. $AgBiS_2$ nanocrystal ink with only water as solvent cannot produce good coverage on SnO_2 substrates. The nanocrystal ink was spin-coated onto SnO_2 substrates at 2000 rpm for 60 s. The nanocrystal films were annealed at 115 °C for 10 min in glovebox. The devices were then stored in desiccator for several days. 2 mg mL^{-1} PTAA in toluene solution was deposited onto $AgBiS_2$ nanocrystal films as hole transport layers. Finally, Kurt J. Lesker Nano36 system was used to evaporate 3 nm MoO_3 and 120 nm Ag through a shadow mask to produce solar cells with an area of 3.1 mm^2. Larger area devices (78.5 mm^2) were also fabricated, while similar J_{sc} was observed as small area devices, larger devices showed lower fill factor, due to the high resistance of ITO substrates. The devices were then characterized in air under ambient conditions. Current–voltage measurements were performed with a Keithley 2400 source meter and a Newport Oriel Sol AAA solar simulator with an AM1.5G filter. The intensity of the solar simulator was calibrated using a Hamamatsu S1336 silicon photodiode. The solar cells were measured with and without masks and no differences in short-circuit current density was observed. The EQE measurements was conducted using a Newport Cornerstone 260 monochromator, a Thorlabs MC2000 chopper, a Stanford Research SR570 pre-amplifier and a SR830 lock-in amplifier. The excitation light was calibrated with Newport 818-UV and 818-IR photodetectors. Measurements of J_{sc} and V_{oc} as a function of light intensity were performed with a Thorlabs neutral light intensity filter wheel. Transient photocurrent and photovoltage of the devices were measured with an in-house-built set-up. The set-up comprises a LED lamp to provide steady state white light bias up to 1 sun, a 637 nm laser and an Agilent 4000X oscilloscope. The V_{oc} of devices was controlled by the light intensity of the LED lamp and the transient voltage induced by laser pulse was controlled within 5% of the V_{oc}. The carrier lifetimes are fitted as: $V = V_{oc} + \Delta V * e^{-\frac{t}{\tau}}$, where V is the transient photovoltage, V_{oc} is the open circuit voltage under various light intensities, ΔV

is the varying amplitude of photovoltage upon illuminating laser, τ is the carrier lifetime.

Bibliography

1. Walther, G.-R. *et al.* Ecological responses to recent climate change. *Nature* **416**, 389–395 (2002).
2. Rosa, E. A. & Dietz, T. Human drivers of national greenhouse-gas emissions. *Nature Clim Change* **2**, 581–586 (2012).
3. Nielsen, K. S., Nicholas, K. A., Creutzig, F., Dietz, T. & Stern, P. C. The role of high-socioeconomic-status people in locking in or rapidly reducing energy-driven greenhouse gas emissions. *Nat Energy* **6**, 1011–1016 (2021).
4. Hausfather, Z. & Peters, G. P. Emissions – the 'business as usual' story is misleading. *Nature* **577**, 618–620 (2020).
5. Louwen, A., van Sark, W. G. J. H. M., Faaij, A. P. C. & Schropp, R. E. I. Re-assessment of net energy production and greenhouse gas emissions avoidance after 40 years of photovoltaics development. *Nat Commun* **7**, 13728 (2016).
6. Net Zero by 2050 – Analysis - IEA. https://www.iea.org/reports/net-zero-by-2050.
7. Allen, T. G., Bullock, J., Yang, X., Javey, A. & De Wolf, S. Passivating contacts for crystalline silicon solar cells. *Nat Energy* **4**, 914–928 (2019).
8. Richter, A. *et al.* Design rules for high-efficiency both-sides-contacted silicon solar cells with balanced charge carrier transport and recombination losses. *Nat Energy* **6**, 429–438 (2021).
9. Liu, W. Light-induced activation of boron doping in hydrogenated amorphous silicon for over 25% efficiency silicon solar cells. *Nature Energy* 13.

10. Major, J. D., Treharne, R. E., Phillips, L. J. & Durose, K. A low-cost non-toxic post-growth activation step for CdTe solar cells. *Nature* **511**, 334–337 (2014).
11. Treharne, R. E. *et al.* Optical Design and Fabrication of Fully Sputtered CdTe/CdS Solar Cells. *J. Phys.: Conf. Ser.* **286**, 012038 (2011).
12. Chirilă, A. *et al.* Highly efficient Cu(In,Ga)Se_2 solar cells grown on flexible polymer films. *Nature Mater* **10**, 857–861 (2011).
13. Bu, T. *et al.* Lead halide–templated crystallization of methylamine-free perovskite for efficient photovoltaic modules. *Science* **372**, 1327–1332 (2021).
14. Chiang, C.-H. & Wu, C.-G. Bulk heterojunction perovskite–PCBM solar cells with high fill factor. *Nature Photon* **10**, 196–200 (2016).
15. Chen, H. *et al.* A guest-assisted molecular-organization approach for >17% efficiency organic solar cells using environmentally friendly solvents. *Nature Energy* **6**, 1045–1053 (2021).
16. Hong, L. *et al.* 18.5% Efficiency Organic Solar Cells with a Hybrid Planar/Bulk Heterojunction. *Advanced Materials*, 2103091.
17. Baek, S.-W. *et al.* Efficient hybrid colloidal quantum dot/organic solar cells mediated by near-infrared sensitizing small molecules. *Nat Energy* **4**, 969–976 (2019).
18. Ding, C. *et al.* Over 15% Efficiency PbS Quantum-Dot Solar Cells by Synergistic Effects of Three Interface Engineering: Reducing Nonradiative Recombination and Balancing Charge Carrier Extraction. *Advanced Energy Materials*, 2201676 (2022).

19. Best Research-Cell Efficiency Chart. https://www.nrel.gov/pv/cell-efficiency.html.
20. Boles, M. A., Ling, D., Hyeon, T. & Talapin, D. V. The surface science of nanocrystals. *Nature Mater* **15**, 364–364 (2016).
21. García de Arquer, F. P. *et al.* Semiconductor quantum dots: Technological progress and future challenges. *Science* **373**, eaaz8541 (2021).
22. Thanh, N. T. K., Maclean, N. & Mahiddine, S. Mechanisms of Nucleation and Growth of Nanoparticles in Solution. *Chem. Rev.* **114**, 7610–7630 (2014).
23. Hines, M. A. & Scholes, G. D. Colloidal PbS Nanocrystals with Size-Tunable Near-Infrared Emission: Observation of Post-Synthesis Self-Narrowing of the Particle Size Distribution. *Advanced Materials* **15**, 1844–1849 (2003).
24. Moreels, I. *et al.* Size-Dependent Optical Properties of Colloidal PbS Quantum Dots. *ACS Nano* **3**, 3023–3030 (2009).
25. Yang, H. *et al.* Au-Doped Ag_2Te Quantum Dots with Bright NIR-IIb Fluorescence for In Situ Monitoring of Angiogenesis and Arteriogenesis in a Hindlimb Ischemic Model. *Advanced Materials*, 2103953.
26. Liu, Z.-Y. *et al.* Breaking through the Size Control Dilemma of Silver Chalcogenide Quantum Dots via Trialkylphosphine-Induced Ripening: Leading to Ag_2Te Emitting from 950 to 2100 nm. *J. Am. Chem. Soc.* jacs.1c06661 (2021) doi:10.1021/jacs.1c06661.
27. Cao, Y., Stavrinadis, A., Lasanta, T., So, D. & Konstantatos, G. The role of surface passivation for efficient and photostable PbS quantum dot solar cells. *Nature Energy* **1**, 16035 (2016).

28. Zhang, J., Gao, J., Miller, E. M., Luther, J. M. & Beard, M. C. Diffusion-Controlled Synthesis of PbS and PbSe Quantum Dots with *in Situ* Halide Passivation for Quantum Dot Solar Cells. *ACS Nano* **8**, 614–622 (2014).
29. Liu, M. *et al.* Hybrid organic–inorganic inks flatten the energy landscape in colloidal quantum dot solids. *Nature Mater* **16**, 258–263 (2017).
30. Wang, Y. *et al.* Room-temperature direct synthesis of semi-conductive PbS nanocrystal inks for optoelectronic applications. *Nat Commun* **10**, 5136 (2019).
31. Konstantatos, G. *et al.* Ultrasensitive solution-cast quantum dot photodetectors. *Nature* **442**, 180–183 (2006).
32. Lu, K. *et al.* High-Efficiency PbS Quantum-Dot Solar Cells with Greatly Simplified Fabrication Processing via “Solvent-Curing”. *Adv. Mater.* **30**, 1707572 (2018).
33. Kovalenko, M. V., Scheele, M. & Talapin, D. V. Colloidal Nanocrystals with Molecular Metal Chalcogenide Surface Ligands. *Science* **324**, 1417–1420 (2009).
34. Aqoma, H. & Jang, S.-Y. Solid-state-ligand-exchange free quantum dot ink-based solar cells with an efficiency of 10.9%. *Energy Environ. Sci.* **11**, 1603–1609 (2018).
35. Ning, Z. *et al.* Quantum-dot-in-perovskite solids. *Nature* **523**, 324–328 (2015).
36. Fan, J. Z. *et al.* Micron Thick Colloidal Quantum Dot Solids. *Nano Lett.* (2020) doi:10.1021/acs.nanolett.0c01614.
37. Johnston, K. W. *et al.* Schottky-quantum dot photovoltaics for efficient infrared power conversion. *Appl. Phys. Lett.* **92**, 151115 (2008).

38. Piliego, C., Protesescu, L., Bisri, S. Z., Kovalenko, M. V. & Loi, M. A. 5.2% efficient PbS nanocrystal Schottky solar cells. *Energy Environ. Sci.* **6**, 3054 (2013).
39. Liu, M., Verma, S. D., Zhang, Z., Sung, J. & Rao, A. Nonequilibrium Carrier Transport in Quantum Dot Heterostructures. *Nano Lett.* **21**, 8945–8951 (2021).
40. Luther, J. M. *et al.* Stability Assessment on a 3% Bilayer PbS/ZnO Quantum Dot Heterojunction Solar Cell. *Adv. Mater.* **22**, 3704–3707 (2010).
41. Rath, A. K. *et al.* Solution-processed inorganic bulk nano-heterojunctions and their application to solar cells. *Nature Photon* **6**, 529–534 (2012).
42. Chuang, C.-H. M., Brown, P. R., Bulović, V. & Bawendi, M. G. Improved performance and stability in quantum dot solar cells through band alignment engineering. *Nature Mater* **13**, 796–801 (2014).
43. Hao, M. *et al.* Ligand-assisted cation-exchange engineering for high-efficiency colloidal $Cs_{1-x}FA_xPbI_3$ quantum dot solar cells with reduced phase segregation. *Nat Energy* **5**, 79–88 (2020).
44. Ling, X. *et al.* 14.1% $CsPbI_3$ Perovskite Quantum Dot Solar Cells via Cesium Cation Passivation. *Advanced Energy Materials* **9**, 1900721 (2019).
45. Swarnkar, A. *et al.* Quantum dot-induced phase stabilization of α-$CsPbI_3$ perovskite for high-efficiency photovoltaics. *Science* **354**, 92–95 (2016).
46. Sanehira, E. M. *et al.* Enhanced mobility $CsPbI_3$ quantum dot arrays for record-efficiency, high-voltage photovoltaic cells. *Sci. Adv.* **3**, eaao4204 (2017).
47. Acharya, S. Lead between the lines. *Nature Chem* **5**, 894–894 (2013).

48. Chen, M. *et al.* Highly stable and efficient all-inorganic lead-free perovskite solar cells with native-oxide passivation. *Nat Commun* **10**, 16 (2019).

49. Ghasemi, M. *et al.* Dual-Ion-Diffusion Induced Degradation in Lead-Free $Cs_2AgBiBr_6$ Double Perovskite Solar Cells. *Advanced Functional Materials*, 2002342.

50. Ji, F. *et al.* Lead-Free Halide Double Perovskite $Cs_2AgBiBr_6$ with Decreased Band Gap. *Angewandte Chemie* **132**, 15303–15306 (2020).

51. Ke, W. & Kanatzidis, M. G. Prospects for low-toxicity lead-free perovskite solar cells. *Nat Commun* **10**, 965 (2019).

52. Ye, T. *et al.* Ambient-Air-Stable Lead-Free $CsSnI_3$ Solar Cells with Greater than 7.5% Efficiency. *J. Am. Chem. Soc.* jacs.0c13069 (2021) doi:10.1021/jacs.0c13069.

53. Wang, C. *et al.* Efficiency improvement of flexible Sb_2Se_3 solar cells with non-toxic buffer layer via interface engineering. *Nano Energy* **71**, 104577 (2020).

54. Wang, Z., Wang, Y. & Konstantatos, G. Highly efficient, ultrathin, Cd-free kesterite solar cells in superstrate configuration enabled by band level tuning via Ag incorporation. *Nano Energy* **94**, 106898 (2022).

55. Huang, P.-C., Yang, W.-C. & Lee, M.-W. $AgBiS_2$ Semiconductor-Sensitized Solar Cells. *J. Phys. Chem. C* **117**, 18308–18314 (2013).

56. Rathore, E. *et al.* Origin of Ultralow Thermal Conductivity in n-Type Cubic Bulk $AgBiS_2$: Soft Ag Vibrations and Local Structural Distortion Induced by the Bi $6s^2$ Lone Pair. *Chem. Mater.* **31**, 2106–2113 (2019).

57. Ju, M.-G., Dai, J., Ma, L., Zhou, Y. & Zeng, X. C. $AgBiS_2$ as a low-cost and eco-friendly all-inorganic photovoltaic material: nanoscale morphology–property relationship. *Nanoscale Adv.* **2**, 770–776 (2020).

58. Bernechea, M. *et al.* Solution-processed solar cells based on environmentally friendly $AgBiS_2$ nanocrystals. *Nature Photon* **10**, 521–525 (2016).

59. Burgués-Ceballos, I., Wang, Y., Akgul, M. Z. & Konstantatos, G. Colloidal $AgBiS_2$ nanocrystals with reduced recombination yield 6.4% power conversion efficiency in solution-processed solar cells. *Nano Energy* **75**, 104961 (2020).

60. Hu, L. *et al.* Enhanced optoelectronic performance in $AgBiS_2$ nanocrystals obtained *via* an improved amine-based synthesis route. *J. Mater. Chem. C* **6**, 731–737 (2018).

61. Bae, S. Y. *et al.* Improved Eco-Friendly Photovoltaics Based on Stabilized $AgBiS_2$ Nanocrystal Inks. *Chem. Mater.* **32**, 10007–10014 (2020).

62. Oh, J. T. *et al.* Water-resistant $AgBiS_2$ colloidal nanocrystal solids for eco-friendly thin film photovoltaics. *Nanoscale* **11**, 9633–9640 (2019).

63. Chen, H.-L. *et al.* A 19.9%-efficient ultrathin solar cell based on a 205-nm-thick GaAs absorber and a silver nanostructured back mirror. *Nature Energy* **4**, 761–767 (2019).

64. Massiot, I., Cattoni, A. & Collin, S. Progress and prospects for ultrathin solar cells. *Nature Energy* **5**, 959–972 (2020).

65. Yuan, W. *et al.* In Situ Regulating the Order–Disorder Phase Transition in $Cs_2AgBiBr_6$ Single Crystal toward the Application in an X-Ray Detector. *Advanced Functional Materials* **29**, 1900234 (2019).

66. Bosson, C. J. *et al.* Cation disorder and phase transitions in the structurally complex solar cell material Cu_2ZnSnS_4. *J. Mater. Chem. A* **5**, 16672–16680 (2017).

67. Chen, W., Dahliah, D., Rignanese, G.-M. & Hautier, G. Origin of the low conversion efficiency in Cu_2ZnSnS_4 kesterite solar cells: the actual role of cation disorder. *Energy Environ. Sci.* **14**, 3567–3578 (2021).

68. Malerba, C., Valentini, M. & Mittiga, A. Cation Disorder In Cu_2ZnSnS_4 Thin Films: Effect On Solar Cell Performances. *Solar RRL* **1**, 1700101 (2017).

69. Kopula Kesavan, J. *et al.* Cation Disorder and Local Structural Distortions in $Ag_xBi_{1-x}S_2$ Nanoparticles. *Nanomaterials* **10**, 316 (2020).

70. Guin, S. N., Banerjee, S., Sanyal, D., Pati, S. K. & Biswas, K. Origin of the Order–Disorder Transition and the Associated Anomalous Change of Thermopower in $AgBiS_2$ Nanocrystals: A Combined Experimental and Theoretical Study. *Inorg. Chem.* **55**, 6323–6331 (2016).

71. Khan, M. D. *et al.* Electrochemical investigation of uncapped $AgBiS_2$ (schapbachite) synthesized using *in situ* melts of xanthate precursors. *Dalton Trans.* **48**, 3714–3722 (2019).

72. Ren, X. *et al. In situ* exsolution of Ag from $AgBiS_2$ nanocrystal anode boosting high-performance potassium-ion batteries. *J. Mater. Chem. A* **8**, 15058–15065 (2020).

73. Kagan, C. R. & Murray, C. B. Charge transport in strongly coupled quantum dot solids. *Nature Nanotech* **10**, 1013–1026 (2015).

74. Wong, J., Omelchenko, S. T. & Atwater, H. A. Impact of Semiconductor Band Tails and Band Filling on Photovoltaic Efficiency Limits. *ACS Energy Lett.* **6**, 52–57 (2021).
75. ElAnzeery, H. *et al.* Refractive index extraction and thickness optimization of $Cu_2ZnSnSe_4$ thin film solar cells. *physica status solidi (a)* **212**, 1984–1990 (2015).
76. *Handbook of optical constants of solids*. (Academic Press, 1998).
77. Manzoor, S. *et al.* Optical modeling of wide-bandgap perovskite and perovskite/silicon tandem solar cells using complex refractive indices for arbitrary-bandgap perovskite absorbers. *Opt. Express* **26**, 27441 (2018).
78. Chen, C. *et al.* Characterization of basic physical properties of Sb_2Se_3 and its relevance for photovoltaics. *Front. Optoelectron.* **10**, 18–30 (2017).
79. Gilmore, R. H. *et al.* Epitaxial Dimers and Auger-Assisted Detrapping in PbS Quantum Dot Solids. *Matter* **1**, 250–265 (2019).
80. Bagus, P. S., Illas, F., Pacchioni, G. & Parmigiani, F. Mechanisms responsible for chemical shifts of core-level binding energies and their relationship to chemical bonding. *Journal of Electron Spectroscopy and Related Phenomena* **100**, 215–236 (1999).
81. Tambo, T. & Tatsuyama, C. XPS Study on the Chemical Shifts of Crystalline III–VI Layered Compounds. *J. Phys. Soc. Jpn.* **54**, 4382–4389 (1985).
82. Green, M. A. & Bremner, S. P. Energy conversion approaches and materials for high-efficiency photovoltaics. *Nature Mater* **16**, 23–34 (2017).

83. Adhyaksa, G. W. P., Johlin, E. & Garnett, E. C. Nanoscale Back Contact Perovskite Solar Cell Design for Improved Tandem Efficiency. *Nano Lett.* **17**, 5206–5212 (2017).

84. Pettersson, L. A. A., Roman, L. S. & Inganäs, O. Modeling photocurrent action spectra of photovoltaic devices based on organic thin films. *Journal of Applied Physics* **86**, 487–496 (1999).

85. Centurioni, E. Generalized matrix method for calculation of internal light energy flux in mixed coherent and incoherent multilayers. *Appl. Opt.* **44**, 7532 (2005).

86. Guillemoles, J.-F., Kirchartz, T., Cahen, D. & Rau, U. Guide for the perplexed to the Shockley–Queisser model for solar cells. *Nat. Photonics* **13**, 501–505 (2019).

87. Akgul, M. Z., Figueroba, A., Pradhan, S., Bi, Y. & Konstantatos, G. Low-Cost RoHS Compliant Solution Processed Photovoltaics Enabled by Ambient Condition Synthesis of $AgBiS_2$ Nanocrystals. *ACS Photonics* **7**, 588–595 (2020).

88. Chen, D. *et al.* Solution-Processed, Inverted $AgBiS_2$ Nanocrystal Solar Cells. *ACS Appl. Mater. Interfaces* acsami.1c17133 (2021) doi:10.1021/acsami.1c17133.

89. Pan, H. *et al.* Advances in design engineering and merits of electron transporting layers in perovskite solar cells. *Mater. Horiz.* 10.1039.D0MH00586J (2020) doi:10.1039/D0MH00586J.

90. Yu, B.-B. *et al.* Heterogeneous 2D/3D Tin-Halides Perovskite Solar Cells with Certified Conversion Efficiency Breaking 14%. *Advanced Materials* 2102055 (2021) doi:10.1002/adma.202102055.
91. Jiang, X. Ultra-high open-circuit voltage of tin perovskite solar cells via an electron transporting layer design. *Nature Communications* 7 (2020).
92. Choi, Y. C., Lee, D. U., Noh, J. H., Kim, E. K. & Seok, S. I. Highly Improved Sb_2S_3 Sensitized-Inorganic–Organic Heterojunction Solar Cells and Quantification of Traps by Deep-Level Transient Spectroscopy. *Advanced Functional Materials* **24**, 3587–3592 (2014).
93. Wu, C. *et al.* Water Additive Enhanced Solution Processing of Alloy $Sb_2(S_{1-x}Se_x)_3$-Based Solar Cells. *Solar RRL* **4**, 1900582 (2020).
94. Jean, J. *et al.* Synthesis cost dictates the commercial viability of lead sulfide and perovskite quantum dot photovoltaics. *Energy Environ. Sci.* **11**, 2295–2305 (2018).
95. Shrestha, A., Batmunkh, M., Tricoli, A., Qiao, S. Z. & Dai, S. Near-Infrared Active Lead Chalcogenide Quantum Dots: Preparation, Post-Synthesis Ligand Exchange, and Applications in Solar Cells. *Angewandte Chemie International Edition* **58**, 5202–5224 (2019).
96. Gong, X. *et al.* Highly efficient quantum dot near-infrared light-emitting diodes. *Nature Photon* **10**, 253–257 (2016).
97. Choi, M.-J. *et al.* Cascade surface modification of colloidal quantum dot inks enables efficient bulk homojunction photovoltaics. *Nat Commun* **11**, 103 (2020).

98. Fischer, A. *et al.* Directly Deposited Quantum Dot Solids Using a Colloidally Stable Nanoparticle Ink. *Advanced Materials* **25**, 5742–5749 (2013).

99. Babayigit, A., Ethirajan, A., Muller, M. & Conings, B. Toxicity of organometal halide perovskite solar cells. *Nature Mater* **15**, 247–251 (2016).

100. Gardner, K. L. *et al.* Nonhazardous Solvent Systems for Processing Perovskite Photovoltaics. *Advanced Energy Materials* **6**, 1600386 (2016).

101. Vidal, R. *et al.* Assessing health and environmental impacts of solvents for producing perovskite solar cells. *Nature Sustainability* **4**, 277–285 (2021).

102. Xiao, Y. *et al.* Eco-Friendly $AgBiS_2$ Nanocrystal/ZnO Nanowire Heterojunction Solar Cells with Enhanced Carrier Collection Efficiency. *ACS Appl. Mater. Interfaces* acsami.0c19435 (2021) doi:10.1021/acsami.0c19435.

103. Kelley, M. L. *et al.* Photoconductive Thin Films Composed of Environmentally Benign $AgBiS_2$ Nanocrystal Inks Obtained through a Rapid Phase Transfer Process. *ACS Appl. Electron. Mater.* **3**, 1550–1555 (2021).

104. Chang, J. *et al.* Ligand-dependent exciton dynamics and photovoltaic properties of PbS quantum dot heterojunction solar cells. *Phys. Chem. Chem. Phys.* **19**, 6358–6367 (2017).

105. Poppe, J., Gabriel, S., Liebscher, L., Hickey, S. G. & Eychmüller, A. A versatile approach for coating oxidic surfaces with a range of nanoparticulate materials. *J. Mater. Chem. C* **1**, 1515 (2013).

106. Jeong, K. S. *et al.* Enhanced Mobility-Lifetime Products in PbS Colloidal Quantum Dot Photovoltaics. *ACS Nano* **6**, 89–99 (2012).

107. Goossens, V. M., Sukharevska, N. V., Dirin, D. N., Kovalenko, M. V. & Loi, M. A. Scalable fabrication of efficient p-n junction lead sulfide quantum dot solar cells. *Cell Reports Physical Science* 100655 (2021) doi:10.1016/j.xcrp.2021.100655.

108. Hens, Z. & Martins, J. C. A Solution NMR Toolbox for Characterizing the Surface Chemistry of Colloidal Nanocrystals. *Chem. Mater.* **25**, 1211–1221 (2013).

109. Yang, Z. *et al.* Colloidal Quantum Dot Photovoltaics Enhanced by Perovskite Shelling. *Nano Lett.* **15**, 7539–7543 (2015).

110. Diedenhofen, S. L., Bernechea, M., Felter, K. M., Grozema, F. C. & Siebbeles, L. D. A. Charge Photogeneration and Transport in $AgBiS_2$ Nanocrystal Films for Photovoltaics. *Solar RRL* **3**, 1900075 (2019).

111. Jiang, Q., Zhang, X. & You, J. SnO_2: A Wonderful Electron Transport Layer for Perovskite Solar Cells. *Small* **14**, 1801154 (2018).

112. Jiang, Q. *et al.* Enhanced electron extraction using SnO_2 for high-efficiency planar-structure $HC(NH_2)_2PbI_3$-based perovskite solar cells. *Nat Energy* **2**, 16177 (2017).

113. Xiong, L. *et al.* Review on the Application of SnO_2 in Perovskite Solar Cells. *Advanced Functional Materials* **28**, 1802757 (2018).

114. Kim, G.-W. *et al.* Hole Transport Materials in Conventional Structural (n–i–p) Perovskite Solar Cells: From Past to the Future. *Advanced Energy Materials* **10**, 1903403 (2020).

115. Su, Z. *et al.* Device Postannealing Enabling over 12% Efficient Solution-Processed Cu_2ZnSnS_4 Solar Cells with Cd^{2+} Substitution. *Advanced Materials* **32**, 2000121 (2020).

116. Lee, J. *et al.* Over 11 % efficient eco-friendly kesterite solar cell: Effects of S-enriched surface of $Cu_2ZnSn(S,Se)_4$ absorber and band gap controlled (Zn,Sn)O buffer. *Nano Energy* **78**, 105206 (2020).

117. Chuang, C.-H. M. *et al.* Open-Circuit Voltage Deficit, Radiative Sub-Bandgap States, and Prospects in Quantum Dot Solar Cells. *Nano Lett.* **15**, 3286–3294 (2015).

118. Pradhan, S. *et al.* Trap-State Suppression and Improved Charge Transport in PbS Quantum Dot Solar Cells with Synergistic Mixed-Ligand Treatments. *Small* **13**, 1700598 (2017).

119. Pradhan, S., Stavrinadis, A., Gupta, S., Christodoulou, S. & Konstantatos, G. Breaking the Open-Circuit Voltage Deficit Floor in PbS Quantum Dot Solar Cells through Synergistic Ligand and Architecture Engineering. *ACS Energy Lett.* **2**, 1444–1449 (2017).

List of publications

Wang, Y.; Kavanagh, S. R.; Burgués-Ceballos, I.; Walsh, A.; Scanlon, D. O.; Konstantatos, G. Cation-disorder Engineering Yields $AgBiS_2$ Nanocrystals with Enhanced Optical Absorption for Efficient Ultrathin Solar Cells. *Nat. Photon.* 2022, 16 (3), 235–241.

Wang, Y.; Peng, L.; Wang, Z.; Konstantatos, G. Environmentally Friendly $AgBiS_2$ Nanocrystal Inks for Efficient Solar Cells Employing Green Solvent Processing. *Advanced Energy Materials* 2022, 12 (21), 2200700.

Burgués-Ceballos, I.; **Wang, Y.**; Akgul, M. Z.; Konstantatos, G. Colloidal $AgBiS_2$ Nanocrystals with Reduced Recombination Yield 6.4% Power Conversion Efficiency in Solution-Processed Solar Cells. *Nano Energy* 2020, 75, 104961.

Burgués-Ceballos, I.; **Wang, Y.**; Konstantatos, G. Mixed $AgBiS_2$ Nanocrystals for Photovoltaics and Photodetectors. *Nanoscale* 2022, 14 (13), 4987–4993.

Wang, Z.; **Wang, Y.**; Konstantatos, G. Highly Efficient, Ultrathin, Cd-Free Kesterite Solar Cells in Superstrate Configuration Enabled by Band Level Tuning via Ag Incorporation. *Nano Energy* 2022, 94, 106898.

Wang, Z.; **Wang, Y.**; Taghipour, N.; Peng, L.; Konstantatos, G. Ag-Refined Kesterite in Superstrate Solar Cell Configuration with 9.7% Power Conversion Efficiency. *Advanced Functional Materials* 2022, 2205948.

Taghipour, N.; Whitworth, G. L.; Othonos, A.; Dalmases, M.; Pradhan, S.; **Wang, Y.**; Kumar, G.; Konstantatos, G. Low-Threshold, Highly Stable

Colloidal Quantum Dot Short-Wave Infrared Laser Enabled by Suppression of Trap-Assisted Auger Recombination. *Advanced Materials* 2022, 2107532.